Double-Difference Relocation and Empirical Green's Function Analysis of Storfjorden Earthquakes

Master of Science Thesis in Geodynamics

Norunn Tjåland

DEPARTMENT OF EARTH SCIENCE

UNIVERSITY OF BERGEN

April 2017

Abstract

On 21 February 2008, an earthquake of magnitude M_w 6.1 occurred in Storfjorden on Svalbard. Since then, more than 2000 earthquakes have been recorded in this region. More recently, on 29 March 2016, an earthquake of magnitude M_w 5.2 occurred close to Edgeøya. This event marks the north-eastern extension of the earthquake sequence.

In this study, in order to improve the initial hypocenter locations, the double-difference relocation method has been applied to earthquakes in the Storfjorden area. In addition, earthquake source parameters are derived applying the empirical Green's function method. By using smaller earthquakes in the sequence as empirical Green's functions, the effects from path, site and instrument are removed from the seismogram of a larger correlated earthquake by deconvolution.

The earthquake relocation reveals at least four NE-SW trending structures, that are steeply dipping to the south-east. Faults of other directions are also indicated from fault plane solutions. However these are not resolved in the relocation of the earthquakes. Stress drop estimates reveal a decrease of static stress drop with decreasing seismic moment.

This indicates that the seismicity in Storfjorden is attributed to a complex tectonic structure that is activated under the present state of stress. Moreover, the non-constant stress drop imply varying fault properties between larger and smaller earthquakes.

Acknowledgements

This master thesis has been carried out at the Department of Earth Science, University of Bergen. First of all, I want to thank my main supervisor Lars Ottemöller for continuously giving feedback. He is a great supervisor and I appreciate the guidance, corrections and useful input. Further, I would like to thank co-supervisor Stéphane Rondenay and Henk Keers for advice and feedback during this study. I also appreciate the help received from Won-Young Kim with the velocity model and double-difference location setup.

Bergen, 27.04.2017

Norunn Tjåland

Contents

1 Introduction

Situated at the north-western corner of the Barents Sea Shelf, the Svalbard archipelago represents an intraplate tectonic environment. It is located to the east of an oceanic spreading ridge, the Knipovich ridge at which a great number of earthquakes are being recorded. Seismic activity also takes place on the archipelago itself, as well as on the nearby continental shelf areas. The intraplate activity is scattered in many areas, but also contains four zones of clustered activity, in Heer Land, Nordaustlandet, Hopen and in Storfjorden, respectively. This has been revealed since the time that seismic monitoring started.

In recent years, high seismic activity has been observed in Storfjorden. The increased activity has taken place in the aftermath of a M_W 6.1 earthquake occurring on 21 February 2008. It is the largest recorded earthquake on Norwegian territory and marks the onset of an intraplate earthquake sequence that is still active. In this thesis, in the light of a more recent M_W 5.2 earthquake, occurring on 29 of March 2016, possibly being the north-eastern extension of the Storfjorden sequence, a reassessment of the Spitsbergen microplate-theory of Savostin and Karasik (1981) is done.

An initial study of the earthquake activity in Storfjorden was carried out by Pirli et al. (2010), who determined a focal mechanism for the M_W 6.1 main event through moment tensor inversion using teleseismic and regional observations. In a later study by Pirli et al. (2013), fault plane solutions for some of the larger aftershocks were obtained, as well as a relocation of the events occurring in the time between 2008 and 2012. Junek et al. (2014) provided additional fault plane solutions based on an improved velocity model obtained through joint inversion of teleseismic receiver functions and regional surface wave dispersion. The moment tensor solutions were used to infer the state of stress in the region. Further work by Ottemöller et al. (2014) used fault plane solutions to invert for stress orientation and managed to improve earthquake locations for events from 2008 until 2014, and identify NE-SW trending linear structures. Also, stress drop values were estimated for larger earthquakes based on measured corner frequencies and seismic moment. Junek et al. (2015) also obtained improved locations and could resolve structures.

The purpose of this thesis is to provide an overview of the Storfjorden sequence from 2008 until 2016. Earthquakes are relocated using the double-difference relocation method

in order to improve the more diffuse catalogue locations. Further improvements are made using cross-correlation techniques. In addition, the correlated events are used in an empirical Green's function analysis to determine source parameters. Eventually, the results are reviewed within the geotectonic context.

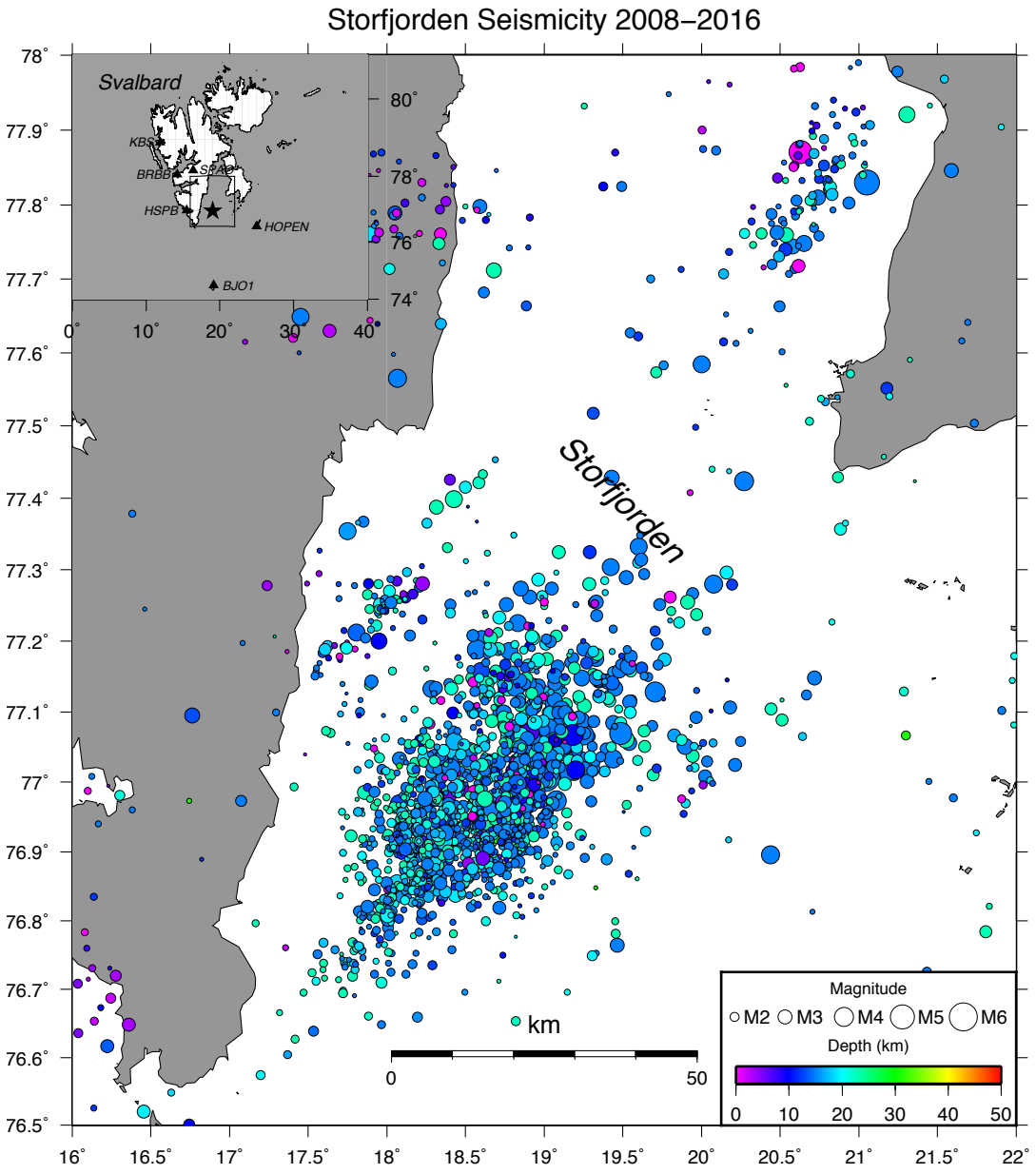

Figure 1.1: Seismicity in Storfjorden 2008-2016 as reported by the Norwegian National Seismic Network, NNSN. Colour indicates hypocenter depth and size scaled with magnitude. The inset shows Svalbard and the locations of seismic stations and study area.

2 Background

2.1 Geologic and tectonic setting

Svalbard has a long geological record and the oldest and most altered rocks belong to the Pre-Caledonian basement. The basement rocks are exposed along the western and northern coast of Svalbard and are of Precambrian (2.5 Ga) to Silurian age (420 Ma). They have been divided into the Northeastern, Northwestern and the Southwestern provinces, and are bounded by major north-south striking fault zones. The basement rocks have been affected by several orogenies, in which the last event was the Caledonian Orogeny that took place from Early Ordovician to Early Devonian (480-400 Ma) during the continental collision of Laurentia and Baltica. It is believed that the three provinces were brought together during the final stage of the Caledonian period (Bryhni et al., 2013).

The Caledonian Orogeny was followed by a change of tectonic regime. After the collision of the continents, the horizontal convergence stopped and extension and orogenic collapse followed. The Caledonian mountains were then exposed to weathering and erosion for a long time and the eroded material accumulated in fault-bounded rift basins. The two Devonian depositional basins, Raudfjorden Basin and Andrée Land Basin, are bounded by the Billefjorden Fault Zone (BFZ) to the east and the Raudfjorden Fault (RF) to the west. During the Late Devonian/Early Carboniferous ($\sim$ 360 Ma) mountain building processes affected an area consisting of the Ellesmere Island, northern Greenland and Svalbard. In Svalbard this event is referred to as the Svalbardian Event. During the Ellesmerian Orogeny, or the Svalbardian Event, the Ny-Friesland basement block to the east was lifted up and thrusted upon the Devonian molasse sediments along the north-south striking Billefjorden Fault Zone. This resulted in folding and thrusting of the adjacent Devonian molasse sediments to the west of the fault (Dallmann, 2015; Piepjohn et al., 2015).

Following the Svalbardian tectonic event, extensional movements along the major, north-south oriented faults controlled sedimentation during Carboniferous (360-300 Ma). This led to development of rift troughs and adjacent highlands, which occur along the Billefjorden and Lomfjorden Fault Zones. Less obvious structures also occur further west, but they have been affected by later tectonic events (Dallmann, 2015).

From Early Carboniferous to the Early Cretaceous (340-145 Ma), the archipelago was mostly submerged and major sedimentary basins, separated by shallow shelf or platform areas, developed over the Barents Sea Shelf. The period was characterized by relatively stable conditions with minor tectonic activity occurring on Svalbard. During the Late Cretaceous, Svalbard emerged from the sea, with subsequent erosion causing the lack(?) of Upper Cretaceous deposits (Dallmann, 2015).

In Early Paleocene ($\sim$ 68 Ma), the first stages of seafloor spreading were initiated in the Labrador Sea and Baffin Bay west of Greenland (Figure 2.1b). This advanced a movement of Greenland towards the north-east and caused the formation of the Eurekan Fold Belt in the northern Ellesmere Island, northern Greenland and in the western part of Svalbard. In Svalbard, the area of Eurekan deformation is often referred to as the West Spitsbergen Fold Belt (WSFB). The fold belt is thought to be part of an intraplate structure which developed in Early Eocene (52 - 45 Ma) (Dallmann, 2015).

During Greenland's north-eastward movement (Figure 2.1c), a large tectonic depression or foreland basin known as the Central Tertiary Basin (CTB) developed east of the fold belt, bounded by the fold belt and the Lomfjorden Fault Zone. This foreland basin developed in response to the formation of the fold belt. The CTB, as well as a rift basin in the North Atlantic Ocean to the west, of which Forlandsundet Graben (FG) was one of the fault blocks where sediments accumulated, were the two depositional basins during the Paleogene (66-23 Ma). In the former, it is believed that a shelf sea emerged from the south-east (Dallmann, 2015).

In the transition from Paleocene to Eocene (56 Ma), active seafloor spreading also occurred in the North Atlantic and in the Eurasian Basin in the Arctic Ocean, and a continental transform fault, the Hornsund Fault Complex (HFC) developed between northern Greenland and the Barents Sea Shelf and Svalbard. While the divergent movement was decreasing in Baffin Bay, seafloor spreading in the North Atlantic and in the Eurasian Basin increased causing the movement of Greenland to the northwest relative to Svalbard along the major Hornsund Fault Complex (Figure 2.1d)

In Late Eocene, seafloor spreading ceased at the western margin of the Greenland plate, but continued in the North Atlantic and in the Arctic Ocean (Figure 2.1e). From Early Oligocene (33 Ma) the continental connection between Greenland and Svalbard was broken and the direction of rifting changed. New transform faults developed (Spitsbergen

and Molloy Fracture Zones) as the transform movement along the HFC ceased and the west coast changed into a passive continental margin. The extension led to the formation of minor sedimentary basins off the western coast of Svalbard, parallel with the Hornsund Fault Complex, in which the best exposed is the Forlandsundet Graben.

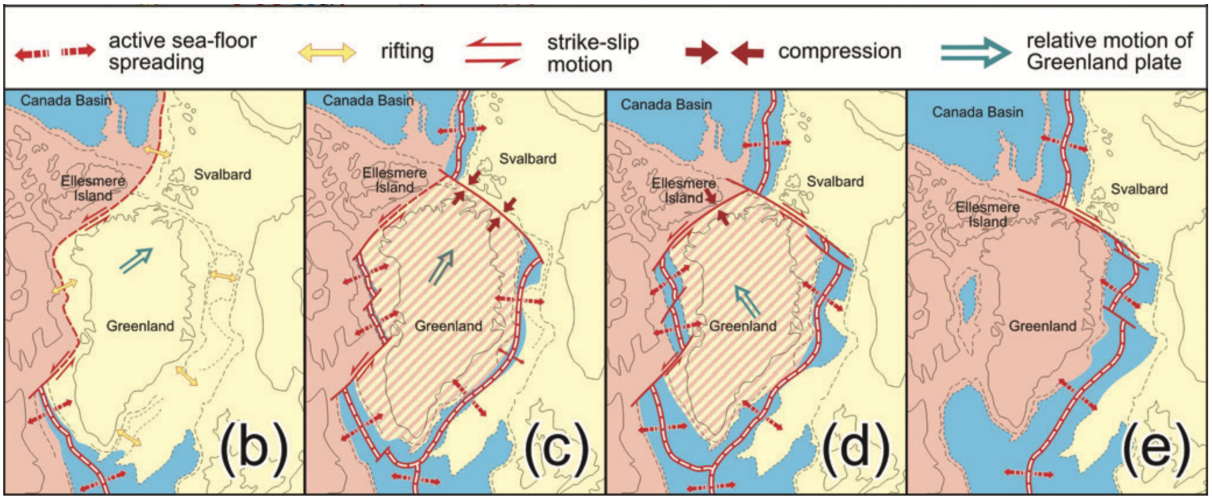

Figure 2.1: Figure showing the different stages of the plate tectonic movements occurring between Early Paleocene and Early Oligocene ($\sim$ 68-33 Ma). (b) The early stages of the Eurekan deformation (68 Ma), where Greenland's movement towards Svalbard has initiated, (c) compressional forces cause the formation of the WSFB and the adjacent foreland basin (56 Ma), (d) Seafloor spreading in the North Atlantic and in the Arctic Ocean cause the change in the relative movement of the Greenland plate and the subsequent development of a continental transform fault between Svalbard and Greenland (47 Ma), (e) Seafloor spreading continuous in the North Atlantic and in the Eurasian Basin and eventually the continental bridge between Svalbard and Greenland is broken (33 Ma) (Piepjohn et al., 2013).

In the time that followed, throughout Neogene (23-2.5 Ma) and Quaternary ($<$ 2.5 Ma), the distance between Greenland and Svalbard increased as the seafloor spreading in the North Atlantic and the Arctic Ocean continued. In the Fram Strait, the deep sea passage between Greenland and Svalbard, the transform faults Spitsbergen and Molloy fracture zones developed (Dallmann, 2015). During Pleistocene (2.5 Ma - 11.7 ka) multiple glaciations occurred. Svalbard had now reached its current position on the northwestern corner of the Barents Sea Shelf, and during the Late Weichselian glacial maximum (LGM) ca. 24,000 to 20,500 years ago, the Svalbard-Barents Sea Ice Sheet reached all the way

Figure 2.2: Geological map of Svalbard (Dallmann, 2015)

to the western shelf edge, covering most of Svalbard and its islands. According to Landvik et al. (1998), the first stages of deglaciation initiated about 15,000 years BP. Rapid recession occurred in western Svalbard, whereas eastern Svalbard did not become ice free before around 10,000 years ago. Since deglaciation, the Barents Sea and Svalbard were no longer covered by an ice sheet, and post-glacial uplift occurred. Higher rates of uplift have been reported in the Barents Sea and on eastern Svalbard, compared to western and northern Spitsbergen (Forman et al., 2004).

The present-day position of the Svalbard archipelago is at the north-western corner of the Barents Sea Shelf (Figure 2.3). It is located in the vicinity of spreading ridges, that is Knipovich Ridge to the west and Gakkel Ridge to the north. Along the Knipovich Ridge slow NW-SE oblique sea floor spreading occurs at a rate of 15 mm/yr in the Norwegian-Greenland Sea. The ridge is bounded by the Mohns Ridge to the south and linked to the Gakkel Ridge through a zone of transform faults, in which the Molloy Fracture Zone and the Spitsbergen Fracture Zone are significant. To the north, in the Arctic Ocean, even slower spreading occurs along the Gakkel Ridge. It is spreading at a rate of about 10 mm/yr (Mitchell et al., 1990; Okino et al., 2002).

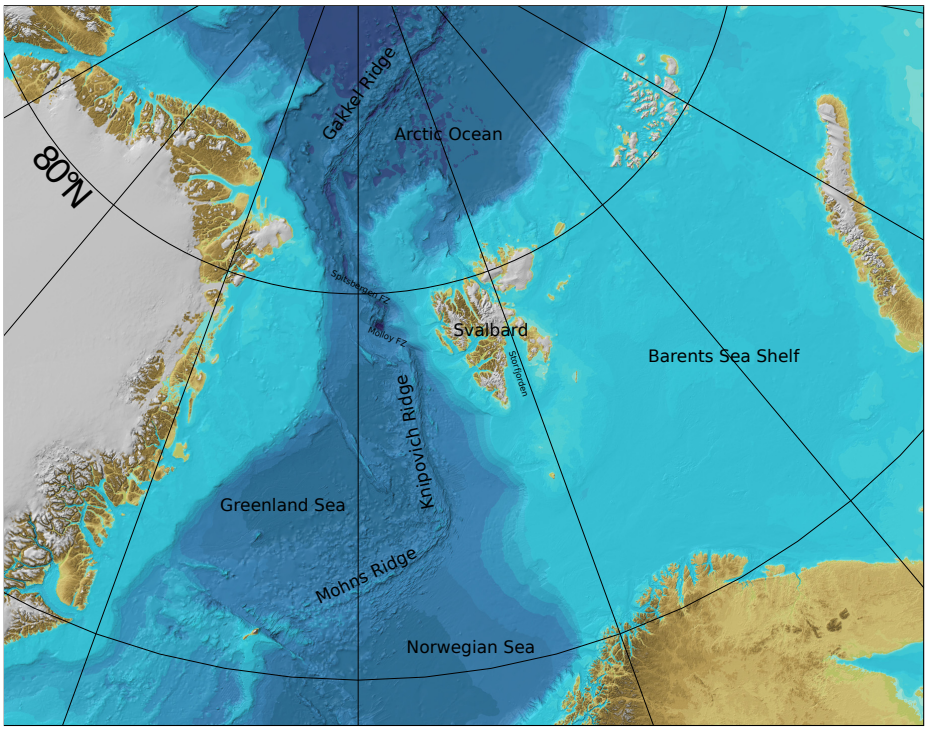

Figure 2.3: Plate tectonic setting of the Svalbard Archipelago showing its intraplate position relative to the spreading ridge to the west (Knipovich Ridge) and to the north (Gakkel Ridge). Modified from Jakobsson et al. (2012).

2.2 Seismicity

Seismicity refers to the distribution of earthquakes in time and space. The seismicity on Svalbard is dominated by concentrated earthquake zones in Heer Land, Nordaustlandet, Hopen and in Storfjorden as reported in previous studies by Mitchell et al. (1979), Bungum et al. (1982), Stange and Schweitzer (2004) and Pirli et al. (2010), respectively. Smaller concentrations, as well as more scattered earthquake activity occur throughout much of the archipelago and on the nearby continental shelf areas. The seismicity along the continental margin can be related to reactivation of old weakness zones remaining from the continental break-up. A high level of seismic activity occurs on the adjacent spreading ridges to the west (Knipovich Ridge) and to the north (Gakkel Ridge) of Svalbard (Figure 2.4). Currently there are six seismic stations for earthquake monitoring located on the Svalbard archipelago, which are installed on the islands of Spitsbergen, Hopen and Bjørnøya (Dallmann, 2015).

2.2.1 Monitoring of seismic activity on Svalbard

During the late 1970s and early 1980s, there was a growing interest in studying the seismicity in Svalbard. In January 1976, a $m_b = 5.6$ earthquake was recorded by teleseismic stations and located in the Heer Land region (Mitchell and Chan, 1978). Prior to 1976, earthquake activity had been reported by the local WWSSN (World-Wide Standardized Seismograph Network) station KBS at Kings Bay in Ny-Ålesund (Austegard, 1976) or from teleseismic stations (Husebye et al., 1975). In 1976 and 1977, temporary seismic networks were established by Saint Louis University. In addition, microearthquake seismographs were installed in 1977 by the Norwegian Polar Research Institute in three of the mining towns of Spitsbergen, as well as a seismic network consisting of seven telemetered stations and three portable microearthquake stations that was in use from late July until the end of August in 1979. The stations were located in southern Spitsbergen, mainly on the east coast close to Heer Land, but also one station was installed southwest on Edgeøya (Bungum et al., 1982).

The monitoring revealed two east-west trending zones of intraplate seismicity; one in Heer Land (HL) and another one in Nordaustlandet (NA) (Bungum et al., 1982). The seismicity in Heer Land was indicating strike-slip movement along an almost vertical WNW-ESE striking fault and the activity was concentrated in the upper crust (Mitchell

et al., 1979). The earthquake activity in Nordaustlandet was associated with a system of mapped faults in the area (Chan and Mitchell, 1985). The largest event recorded in Nordaustlandet during the summer of 1979 was a M_L 3.9 magnitude event (Bungum et al., 1982). The earthquakes were thought to be related to plate tectonic stresses (Mitchell et al., 1990). A more recent event occurred close to Hopen on 4 July in 2003, with an estimated m_b 5.7 magnitude (Stange and Schweitzer, 2004) and with a normal fault mechanism indicating north-south extension (Dallmann, 2015). Today, the highest activity is seen in Storfjorden following the magnitude M_w 6.1 event. The earthquake mechanism varies from pure strike-slip to pure normal faulting (Ottemöller et al., 2014).

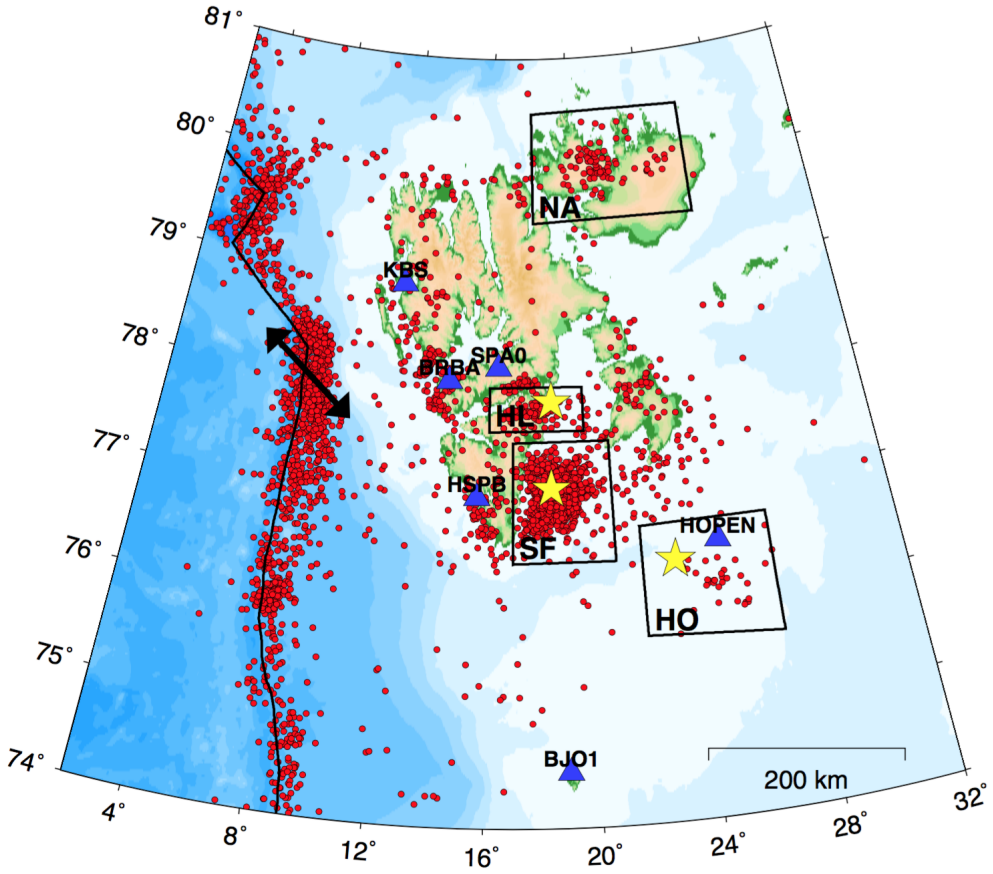

Figure 2.4: Seismicity on the Svalbard archipelago and nearby continental shelf areas and locations of seismic stations (blue triangles). Figure from: Ottemöller et al. (2014).

2.2.2 Stress generating mechanisms

The Svalbard archipelago has an intraplate tectonic setting, but located very close to a passive continental margin. High seismic activity occurs along the Knipovich Ridge

to the west while intraplate seismicity is observed across the margin. The transform movement between Svalbard and Greenland during the Eurekan tectonic event are likely to have created zones of weakness along the margin, which are being reactivated under the current stress system.

Seismicity along and across the margin can vary, indicating that it is influenced by both regional and local factors (Stein et al., 1989). Sources of stress might be plate tectonic stresses, including ridge push, that will cause compressive forces mostly normal to the margin and capable of stresses of an order of magnitude up to 10-20 MPa depending on age (Hicks et al., 2000), or continental margin spreading which is caused by differences in density between continental and oceanic lithosphere and can explain continental extension and oceanic compression normal to the margin (Stein et al., 1989).

More regional factors are flexural stresses due to unloading/loading processes which is another source of stress that can explain tensional stresses. Sediment loading along margins has the potential of creating stresses up to 100 MPa if deposited within a relatively short period of time (Stein et al., 1989). The removal of a large ice-sheet is also believed to give rise to flexural stresses which can influence on the seismicity in recently deglaciated regions. In coastal regions in northern Norway, there are indications that post-glacial isostatic uplift might be the explanation of shallow, normal faulting and swarm related earthquakes (Bungum et al., 2010; Hicks et al., 2000). Depending on size, topographic loads may also contribute to local and regional stress (Fejerskov and Lindholm, 2000).

3 Methods and Theory

This chapter is divided into two sections, one will give the theoretical background for the double-difference relocation method, which is implemented in the hypoDD program, while the other will explain the empirical Green's function method that is used to estimate earthquake source parameters.

3.1 Earthquake location

Earthquake location is an inverse problem where observed arrival times of seismic waves at different stations are used to determine hypocenter location and origin time (Figure 3.1). Errors of measurement or systematic errors due to uncertainties in the velocity model can have a large effect on the accuracy of the earthquake locations. Station geometry or errors in station parameters may also introduce location uncertainties. Another potential problem is misidentification of seismic phases which will result in a wrong travel time curve for the observed phase and cause problems when attempting to minimize the residual between observed and calculated travel times. Many location programs use only first arrivals (e.g., hypoDD) (Waldhauser, 2001) and that might introduce difficulties at certain distances where the direct Pg/Sg-phase arrive close in time to the upper mantle Pn/Sn-phase which usually has a small amplitude and can easily be missed (Havskov and Ottemöller, 2010). On Svalbard, the Pn-phase can often be missed on noisy stations (e.g. BJO1). Also, very few observations of Sn-phases for stations KBS and BJO1 (Ottemöller et al., 2014).

A conventional way of locating earthquakes is based on a linearised, iterative approach, which will provide a hypocenter location and origin time and gives the smallest residuals between the observed and calculated arrival time. This approach is computationally fast and can be used for both traditional single-event location and in relative location methods (Havskov and Ottemöller, 2010; Husen and Hardebeck, 2010). However, there are some limiting factors that are important to be aware of when using this technique when solving the earthquake location problem, and these will be further explained in the following sections.

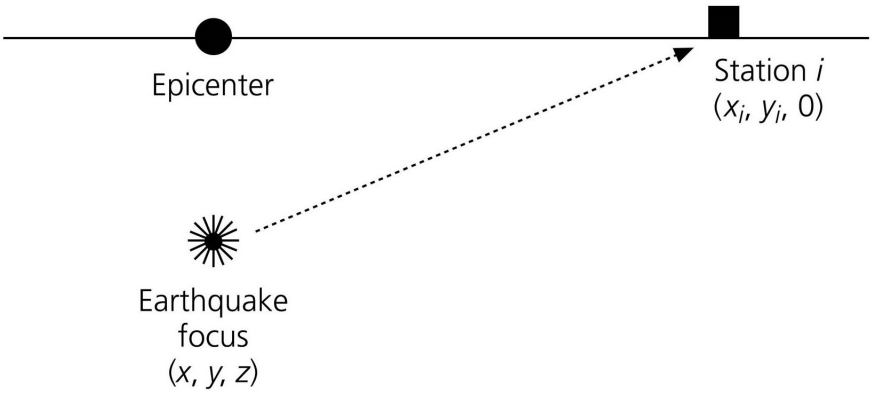

Figure 3.1: Illustration of the earthquake location problem where arrival times, recorded at known station location $(x_i, y_i, 0)$, are used to estimate the unknown hypocentral parameters (x, y, z, τ) (Stein and Wysession, 2003).

3.2 Single-event location

The traditional way of locating earthquakes gives absolute locations by determining locations for one event at a time. As mentioned, the data used for earthquake locations are a number of arrival times measured for different phases which are being recorded by a network of seismic stations. The observed arrival time depends on the origin time and the travel time between hypocenter and station. Thus, the velocity structure is crucial (Stein and Wysession, 2003).

The first step in the location process is to make a guess of a hypocenter location and origin time, that will represent a starting model that we assume is close to the true solution. The starting model will give calculated arrival times, t^{cal}, that we want to be close to the observed arrival times, t^{obs}. The calculated arrival times will differ from those that were actually observed. Therefore, we seek changes in the starting model that will make the calculated data closer to the observed data.

Since the relationship between travel time and earthquake location is nonlinear, a Taylor series expansion of the equation about a starting model is applied to linearise. In order to linearise the problem, it is assumed that the estimated hypocenter is not too far from the true value, such that the travel time residual between the observed and calculated travel time, $r_k^i = (t^{obs} - t^{cal})_k^i$, for an earthquake i, will be linearly related to adjustment in the hypocentral parameters $\Delta\mathbf{m}^i$, through the partial derivative of the travel time with respect to the unknown model vector $\mathbf{m}$ (Waldhauser and Ellsworth, 2000).

$$\frac{\partial t_k^i}{\partial \mathbf{m}} \Delta \mathbf{m}^i = r_k^i \tag{3.1}$$

Equation (3.1) can be written as a system of linear equations $\mathbf{Gm} = \mathbf{d}$ where $\mathbf{d}$ is the residual vector, $\mathbf{m}$ is the adjustment vector for the hypocentral parameters and $\mathbf{G}$ is the matrix containing the partial derivatives. The system consists of four unknown hypocentral parameters and one equation for each arrival time observation. It will often be more equations than unknowns. Due to errors, this overdetermined system is almost always inconsistent and there will be no exact solution (Stein and Wysession, 2003). Therefore, we try to obtain the best possible solution and that can be done using standard least squares techniques. The starting model is then corrected according to the misfit and a new model will then be used as a starting model for the next iteration. The process will be repeated until a defined convergence criteria is reached (Figure 3.2).

Usually, iterative location programs find the initial value at a station recording the first arrival. With good station coverage and with an epicenter that is close or within the network, this will be sufficient in most cases. However, if the quality of the initial guess is poor or the data is not well constrained, the solution might converge slowly or not at all. It may also only converge to a local minimum (Havskov and Ottemöller, 2010; Husen and Hardebeck, 2010).

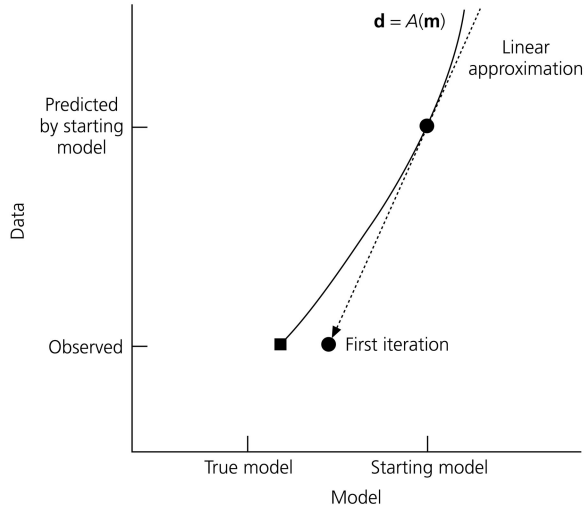

Figure 3.2: Schematic illustration of the linearised location method. The approximation will get closer to the true solution by minimizing the residual between the observed and predicted data (Stein and Wysession, 2003).

3.3 Double-difference earthquake location

Instead of locating earthquakes one at a time, earthquakes can be located either relative to a master event or relative to each other. Typical approaches include Joint Hypocenter Determination (Douglas, 1967) and Bayesian location (Myers et al., 2007). In this study, the double-difference earthquake location algorithm, developed by Waldhauser and Ellsworth (2000) will be applied. It combines absolute travel-time differences obtained from earthquake catalogues with differential travel times derived from waveform cross-correlation. Instead of minimizing the residual between observed and calculated travel times for single events, the algorithm reduces the difference between observed and calculated travel time differences (or double-differences) for pairs of earthquakes. By combining the two different types of data, the relative locations between clusters and uncorrelated events depend on the accuracy of the catalogue data, while the distances between events within clusters depend on the accuracy of the cross-correlation data. In areas of dense seismicity this method can greatly improve the seismicity image by resolving fault lines (Waldhauser and Ellsworth, 2000).

The double-difference method assumes that the ray paths of two event, i and j, will be almost the same if the hypocentral distance between the two events is small compared to the distance between the event and a common station, k. Then, the travel time difference between two events observed at a common station will be due to the spatial offset between the two events (Figure 3.3) and any effects from velocity heterogeneities will cancel out, except from in a small region between the two events where the ray path is different (Waldhauser and Ellsworth, 2000).

The double-difference, or the residual between observed and calculated travel time difference for earthquake pairs, is given by equation (3.2).

$$dr_k^{ij} = (t_k^i - t_k^j)^{obs} - (t_k^i - t_k^j)^{cal} \tag{3.2}$$

The double-difference equation is linearised and the resulting problem is then one in which the residual for events i and j, recorded at station k, is linearly related to perturbations, $\Delta\mathbf{m}^i$ and $\Delta\mathbf{m}^j$, of their hypocentral parameters, through the partial derivatives of the travel times for each event with respect to the unknown, represented by $\mathbf{m}$ in equation:

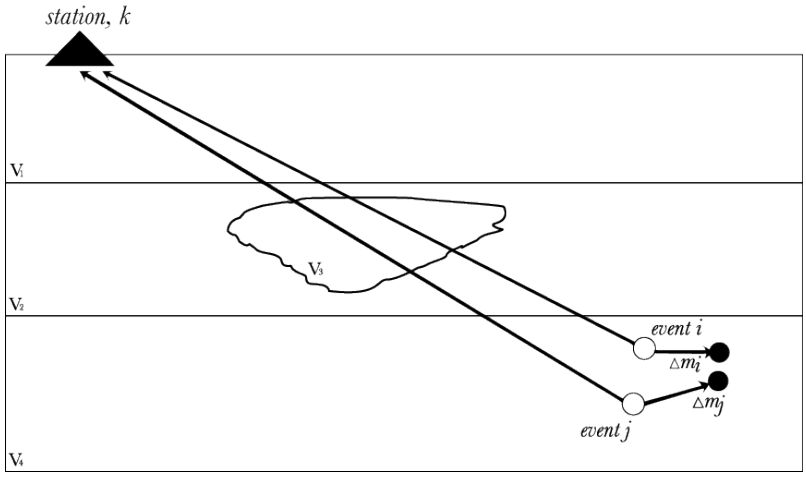

Figure 3.3: Illustration of double-difference method where two events, i and j, have almost identical ray path from source to receiver, due to the small hypocentral separation between them. The inter-event distance of initial locations (open circles) are reduced after relocation (solid circles). Modified from Waldhauser and Ellsworth (2000); Castellanos and van der Baan (2013).

$$\frac{\partial t_k^i}{\partial \mathbf{m}} \Delta \mathbf{m}^i - \frac{\partial t_k^j}{\partial \mathbf{m}} \Delta \mathbf{m}^j = dr_k^{ij} \tag{3.3}$$

written out in full,

$$\frac{\partial t_k^i}{\partial x} \Delta x^i + \frac{\partial t_k^i}{\partial y} \Delta y^i + \frac{\partial t_k^i}{\partial z} \Delta z^i + \Delta \tau^i - \frac{\partial t_k^j}{\partial x} \Delta x^j - \frac{\partial t_k^j}{\partial y} \Delta y^j - \frac{\partial t_k^j}{\partial z} \Delta z^j - \Delta \tau^j = dr_k^{ij} \tag{3.4}$$

or, in matrix notation,

$$\mathbf{G}\mathbf{m} = \mathbf{d} \tag{3.5}$$

where the partial derivative matrix $\mathbf{G}$, is of size $M \times 4N$, where M is the number of double-difference observations and N is the number of events; $\mathbf{d}$ is the data vector of double-difference residuals for all event pairs; $\mathbf{m}$ is a vector of length $4N$ containing the changes in the hypocentral parameters $(\Delta x, \Delta y, \Delta z, \tau)$ that are being solved for (Waldhauser and Ellsworth, 2000).

The system expressed by equation (3.5) can be solved in a weighted least-square sense using normal equations which will give the least square solution $\hat{\mathbf{m}}$:

$$\hat{\mathbf{m}} = (\mathbf{G^T W^{-1} G})^{-1} \mathbf{G^T W^{-1} d} \tag{3.6}$$

where $\mathbf{W}$ contains the *a priori* quality weights which depend on the quality of the data. More specifically, the quality of the arrival time measurement for the catalogue data and the quality of the correlation measurement for cross-correlated data.

For small, well-constrained clusters, equation (3.5) can be solved by using the method of singular value decomposition (SVD):

$$\hat{\mathbf{m}} = \mathbf{V \Lambda^{-1} U^T d} \tag{3.7}$$

As the system becomes larger and the SVD method cannot handle large amounts of data, a more efficient way of finding the solution $\hat{\mathbf{m}}$ is by using the conjugate gradient algorithm LSQR, which is applicable to sparse systems and solves the damped least square problem:

$$\left\| \mathbf{W} \begin{bmatrix} \mathbf{G} \\ \lambda \mathbf{I} \end{bmatrix} \mathbf{m} - \mathbf{W} \begin{bmatrix} \mathbf{d} \\ \mathbf{0} \end{bmatrix} \right\|_2 = 0 \tag{3.8}$$

The initial solution to equation (3.5) is taken from the starting locations and the *a priori* weights. The process continuous in an iterative manner, in which the residuals, locations and partial derivatives are updated after each iteration. The *a priori* weights are applied until a stable solution has been obtained. Typically, this is achieved in 2-3 iterations using SVD and 5 using LSQR. In the iterations that follow, the data is reweighted by multiplying the *a priori* weights with misfit weights that reject or downweight observations with large residuals, and with distance weights that downweight data for event pairs with large inter-event distances. The iterations stop when the RMS residual reaches a certain threshold value that depend on the noise level of the data, when the adjustment in the hypocentral parameters is below a chosen threshold, or when the number of iterations have reached its maximum (Waldhauser and Ellsworth, 2000).

3.4 Earthquake relocation using hypoDD

HypoDD is a computer program that implements the double-difference earthquake location algorithm, developed by Waldhauser and Ellsworth (2000). The relocation process is performed by running the two programs *ph2dt* and *hypoDD*, which forms absolute travel time differences from earthquake catalogues for event pairs and then use the double-difference relocation algorithm to locate the earthquakes. In *hypoDD* one can combine catalogue data with cross-correlated data. These data are formed in the SEISAN program CORR, which gives differential travel times for event pairs at common stations, and can further be used as input to *hypoDD*.

3.4.1 Data preprocessing using ph2dt

The first step is to create a file (dt.ct) that stores absolute travel times from earthquake catalogues for earthquake pairs observed at a common station. This is done in the preprocessing program *ph2dt* which uses files containing information about station location (station.dat) and catalogue travel time data (phase.dat). For this study, these files were created by the program NOR2DD which uses the Nordic and STATION.HYP files to produce the input files for hypoDD (Ottemöller, Voss and Havskov, 2014). In addition, a control file (ph2dt.inp) sets the parameter values to control the program run. These values control the forming of event pairs and the input to *hypoDD*. The phase data are assigned weights with a value between 1 and 0, and when the catalogue data is formed the minimum pick weight MINWGHT is set to 0 in order to consider all available phase pairs. As mentioned, accurate arrival times are critical for location precision. However, location uncertainties can be reduced using waveform cross-correlation data (Waldhauser and Ellsworth, 2000), as described in the next section.

In areas of dense seismicity, a network of earthquakes can be established. Event pairs can be linked to neighbouring events such that a continuous chain of event pairs that are located in close proximity to each other are formed. The maximum hypocentral separation between an event pair, MAXSEP, should be small in comparison to the distance between an event pair and station, given by MAXDIST. Each event can be linked to a maximum of MAXNGH neighbouring events that occur within the search radius and meets the minimum number of phase pair links, MINLNK. Phase pairs that have at least eight observations would typically be considered as a strong link, because there is at least one

observation for the eight degrees of freedom. Also, a minimum or maximum number of selected links per pair can be specified under, MINOBS and MAXOBS, respectively (Waldhauser, 2001). With the sparse station distribution on Svalbard it is a challenge to obtain enough links per pair to form strongly linked events, and therefore it is necessary to allow phase pairs that have less than eight observations, but more than four.

After each run, the program will produce a log file (ph2dt.log) that stores information about the linking of events. The number of linked event pairs will be reported, the number of weakly linked events, as well as the average number of links per pair. The average offset between strongly linked events are also given, and should be considered when more conservative values for the hypocentral separation between two events, through WDCT, are used in *hypoDD*. The log file also reports outliers that have been removed after running *ph2dt* (Waldhauser, 2001).

3.4.2 Waveform correlation using CORR

Cross-correlation can be used to measure waveform similarity, and high correlation may indicate similar focal mechanism and closely spaced hypocenters (Schaff et al., 2004). CORR is a program in the earthquake analysis software, SEISAN, which creates the input file (dt.cc) for *hypoDD*. This file stores differential travel times for pairs of earthquakes and weights ranging from 0-1 according to the squared coherency. These are the *a priori* weights assigned for the cross-correlation data (Ottemöller, Voss and Havskov, 2014; Waldhauser and Ellsworth, 2000).

The similarity between two signals x and y can be measured by the cross-correlation function r_{xy} given in equation (3.9) (Ottemöller, Voss and Havskov, 2014). Highly accurate arrival times for both P and S-phases can be determined for similar waveforms through cross-correlation.

$$r_{xy}(i) = \frac{\sum_{j=1}^{n} x_j y_{(j+i-1)}}{\sqrt{\sum_{j=1}^{n} x_j^2} \sqrt{\sum_{j=1}^{n} y_{j+i-1}^2}} \tag{3.9}$$

The program can cross-correlate all events in the input file. Either the whole trace or a selected phase window can be used. The time for which the function gives the maximum correlation, is where the waveforms are most similar and this will determine the phase arrival time. A minimum correlation value will be set in the input file (corr.inp). Filtering

of the data can be activated and it is usually necessary when including events of different magnitudes. It is possible to search for correlated events among all events and then find groups of similar events in the group identification mode (Ottemöller, Voss and Havskov, 2014).

3.4.3 Clustering and earthquake relocation using hypoDD

Once the catalogue data (dt.ct) and the cross-correlation data (dt.cc) have been created, they can be used separately or combined in *hypoDD*. The data type and phases to be used can be specified in the control file (hypoDD.inp) under IDAT and IPHA, respectively.

Before solving the least squares problem, events are grouped into clusters to ensure stability of the inversion. A continuous cluster of linked event pairs are formed when a minimum number of cross-correlation links, OBSCC, or catalogue links, OBSCT, for each event pair are reached. Similar to the MINLNK parameter, eight observations would usually be an appropriate threshold value. The number of events included in one cluster will also depend on the distance, DIST, between the cluster centroid and station. In hypoDD, the size of the cluster can be as small as one event pair or as large as possible depending on the number of events. All clusters can be relocated simultaneously or individually (Waldhauser, 2001).

HypoDD gives two options for solving the system of double-difference equations, either by singular value decomposition (SVD) or conjugate gradient least squares method (LSQR). The choice on method will be defined under ISOLV and will depend on size and condition of the system. For small and well-conditioned systems, SVD can be used. While for larger, sparse systems it is more efficient to use LSQR. When solving the system in LSQR mode, the final output should be critically assessed. Especially in case of azimuthal gap or sparse station distribution, the quality of the solution should be carefully evaluated (Waldhauser, 2001).

The double-difference algorithm will solve the system in an iterative manner and the number of iterations, specified under NITER, will depend on the initial locations and how well constrained the system is. The initial locations are obtained from the earthquake catalogue or from the cluster centroid and set under ISTART. The condition of the system will be indicated by the condition number CND. Weakly linked events or outliers will increase this number and it might be necessary to damp the solution with a damping

factor DAMP. Damping is only possible when using LSQR. For each set of iterations, a different damping value can be assigned. This value should be adapted to the resulting condition numbers in the *hypoDD* output. According to Waldhauser (2001), a damping factor between 1 and 100, with condition number between 40 and 80 will be desirable when solving with LSQR.

An important part of the relocation process is weighting and re-weighting of data. The different types of data are assigned with *a priori* weights according to the quality of the data. The catalogue data are given relative weights depending on the precision of the arrival time measurements, while the cross-correlation data have weights that depend on the precision of the cross-correlation measurement. When the two data types are combined, the catalogue data is often down-weighted relative to the more precise cross-correlation data (Waldhauser and Ellsworth, 2000). In many cases, P-phases will also be given larger weights than S-phases (Havskov and Ottemöller, 2010). The relative *a priori* weights can be specified under WTCCP, WTCCS, WTCTP and WTCTS. In addition to these quality weights, the data is re-weighted with weights that depend on the misfit and event separation. This will remove or down-weight outlier data which have a residual larger than the cut-off value, given in seconds or as a factor to be multiplied with the standard deviation. It will also remove events that are separated by a distance that exceeds a certain threshold (Waldhauser, 2001). These weights are specified under WRCC, WRCT, WDCC and WDCT. By using different weights for the data, event pairs with large separation distances can be controlled by the catalogue data, while event pairs with small separation distances can be controlled by the cross-correlation data.

The *hypoDD* output gives information about the relocation for each iteration. It reports the number of successful iterations and those that are repeated due to airquakes, in the first two columns (IT). The third column (EV) will inform on the percentage of events that are used in each iteration, while column number four (CT) and five (CC) will specify the percentage of catalogue and cross-correlation data used in each step. During the relocation, events will be removed if they are not well connected or if they locate above ground as airquakes. The number of events that are discarded will be indicated from these values and is useful for deciding proper weighting and the quality of the data. The double-columns (RMSCT) and (RMSCC) gives the RMS residual for the two data types in ms and the change in percent from the previous iteration. This number is expected to

decrease as the data becomes more confined. The following column (RMSST) reports the largest residual observed at one station. The average absolute change for the hypocentral parameters for each iteration is given in column nine to twelve (DX, DY, DZ, DT). These values are expected to decrease with each iteration until the noise level of data has been reached. If the solution is not converging, the damping might be too high or the system might be poorly constrained. On the other hand, very large changes might be caused by too low damping. Column thirteen (OS) is the absolute shift of the initial location and the relocation of the cluster centroid. It is desirable with only smaller changes for this value. Column fourteen (AQ) reports airquakes. A large number of airquakes might be due to an inappropriate velocity model or underdamping. The final column (CND) indicates the condition of the system. This run time information will be stored in the *hypoDD* log file (hypoDD.log) (Waldhauser, 2001).

3.4.4 Application to the Calaveras fault

The *HypoDD* program includes three sets of sample data. One of them being a collection of 308 events recorded at the Calaveras fault, a major branch of the San Andreas fault. I used this data set to test and demonstrate the performance of the double-difference relocation algorithm. The relocation method collapses the more diffuse catalogue locations and reveals narrow linear features associated with tectonic structures.

Travel-time differences for event pairs with a hypocentral separation of less than 15 km at stations that are present within a radius of 500 km are formed. Each event has been linked to a maximum of 15 neighbouring events that locate within the search radius. A minimum number of eight links is used to define a neighbour. A minimum number of eight links and a maximum number of 50 links per pair is saved. A total of 65,913 P-phase and 543 S-phase pairs are selected. The number of linked event pairs is 2957 and each pair has an average of 22 links. The average distance between strongly linked events is 0.246 km, indicating a dense hypocenter distribution. In addition to the catalogue data, differential travel-times from cross-correlation data are used, resulting in 58,518 P and 41,256 S differential times. One cluster containing all 308 events are formed and relocated as there were no weak links. The program was run multiple times with different values for the parameters that control the program. The data set is proven to be very robust and not sensitive to changes in these parameters. For instance, large changes in the maximum

hypocentral distance did not make any significant changes.

The earthquakes were relocated using only catalogue data (Figure 3.4) and by combining catalogue data with cross-correlation data (Figure 3.5). The relocations, when performed on only the catalogue data show a much more diffuse seismicity pattern both in map view and in the cross section. When both the catalogue and cross-correlation data are used in the relocation, narrow and more defined zones of seismic activity are revealed.

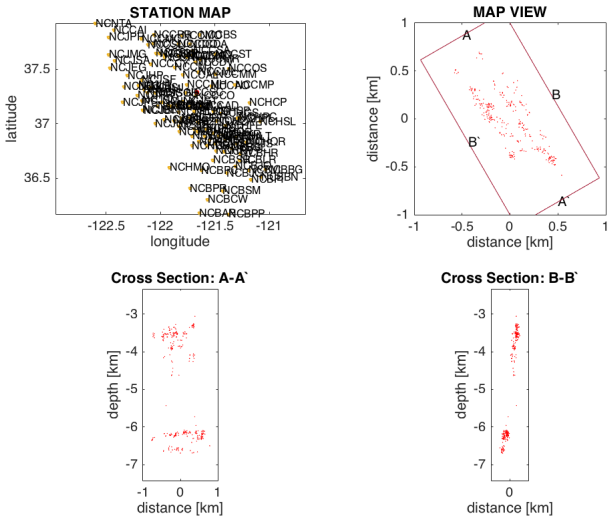

Figure 3.4: HypoDD relocation with only catalogue data.

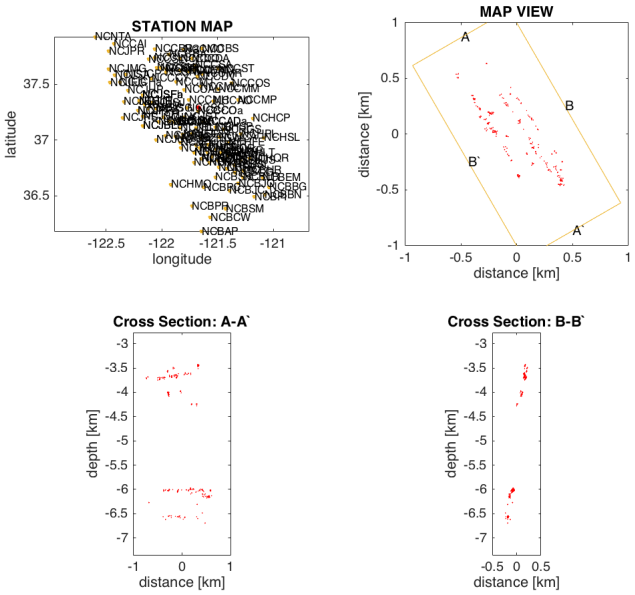

Figure 3.5: HypoDD relocation combining cross-correlation data with catalogue data.

3.5 Earthquake source parameters

Previously, I have used arrival times of seismic waves recorded at different stations to find the hypocenter location of the earthquakes. Next, as discussed in this part, I will retrieve information about the earthquake faulting from the generated seismic waves. An important factor in describing the earthquake source process is the source time function. The recorded seismogram shows the combined effect of the earthquake source, the earth structure, and the instrument response. Thus, a seismogram, $u(t)$, is given by the convolution of each function in the time domain, which can be written:

$$u(t) = x(t) * e(t) * q(t) * i(t), \tag{3.10}$$

where $x(t)$ is the source time function, $e(t)$ and $q(t)$ contains information about the earth structure and $i(t)$ is the instrument response. More specific, $e(t)$ gives the effects of elastic wave phenomena like reflections of waves, the conversion of waves at interfaces along its ray path, and geometrical spreading. While, $q(t)$ describes the anelastic attenuation, in which some of the mechanical energy is converted into heat. Convolution in the time domain is equivalent to multiplication in the frequency domain and equation (3.10) can be written as the product of the Fourier transforms of the four functions.

$$U(\omega) = X(\omega) \cdot E(\omega) \cdot Q(\omega) \cdot I(\omega) \tag{3.11}$$

3.5.1 Finding clusters of correlated events with XCLUST

By using correlated earthquakes in the empirical Green's function analysis it is assumed that the EGF has comparable mechanism to the larger earthquake, and that the path and site effects are similar for both events. XCLUST is a program in SEISAN used for cluster analysis. The output file (cc.pairs.out) from the cross-correlation program CORR (see subsection 3.4.2) gives a list of correlated event pairs, with their respective index and s-files, as well as the average correlation of all stations and the number of recording stations. This file can further be used as the input file to XCLUST, which will divide the data into groups of similar events. The program will first put the data in an order according to the correlation of each event pair. Event pairs of high correlation are put into

the same group, or cluster, and more events can be added if they are linked with events in this cluster. When there is no more events to be added to the group, the search for a new group continuous. The output file (xclust.out) contain information on the number of clusters, the number of events within each cluster and how each event is linked to the other events in the same group (Ottemöller, Voss and Havskov, 2014).

3.5.2 Empirical Green's function method

The purpose of many studies is to isolate the source time function of an earthquake of interest. This can be accomplished by using the empirical Green's function method introduced by Mueller (1985). Small earthquakes can be used as an empirical Green's function (EGF) to remove path, site and instrument effects from the seismogram of a larger earthquake, provided that the two earthquakes are collocated, recorded on the same station, and that the EGF approximates a delta function in the frequency band of interest. The method has proven to be especially useful in determining source parameters for earthquakes of small magnitudes, in which the corner frequency often will be within the range of frequencies most affected by geometrical spreading and near surface attenuation (Hartzell, 1978; Mori and Frankel, 1990), but it can also be applied to larger earthquakes (Benz and Herrmann, 2014).

The effects from path, site and instrument can be removed by spectral division in the frequency domain by dividing the spectra of the larger event, $R(\omega)$, by the spectra of the smaller event, $Z(\omega)$, defined as an empirical Green's function (equation 3.12). The deconvolution becomes unstable if zeroes or very small values are present in the denominator. One common technique to avoid instability and errors in the results is by adding a water-level (Clayton and Wiggins, 1976). This will replace any zeroes or small values in the denominator, the spectra of the EGF, with a value corresponding to the water-level parameter c. This parameter will be a fraction of the maximum amplitude of $Z(\omega)$ in which it is multiplied with (equation 3.13). This will prevent the spuriously high amplitudes that may appear if dividing by small values. (*) denotes complex conjugates as the water-level method will introduce negative parts that are not real (Ammon, 1991; Vallée, 2004).

$$H(\omega) = \frac{R(\omega)Z^*(\omega)}{\phi(\omega)}G(\omega) \tag{3.12}$$

$$\phi(\omega) = max\{Z(\omega)Z^*(\omega), c \cdot max\{Z(\omega)Z^*(\omega)\}\}, \tag{3.13}$$

$$G(\omega) = \xi \, exp\left(\frac{-\omega^2}{4a^2}\right) \tag{3.14}$$

The source time function is multiplied by the transform of a Gaussian filter (equation 3.14). This is done in order to remove noise and control the bandwidth. ω is frequency in radians and a is the alpha parameter controlling the width of the Gaussian. The larger the alpha parameter is, the greater the bandwidth, and the more details of the deconvolved source time functions are kept (Langston, 1979; Velasco et al., 2000). The constant ξ will normalize the Gaussian filter according to the amplitude (Ammon, 1991).

3.5.3 Deconvolution in DECON

DECON is a program in SEISAN which performs the water-level deconvolution. The aforementioned factors controlling the deconvolution, that is, the water-level and the Gaussian width, can be controlled in the input file (decon.inp). This file contain all the correlated events for each cluster, where the earthquake of interest is defined as a master event, while the others are the smaller events used as EGFs. The deconvolution will be done for all the listed events. The phase to consider (either P or S), the duration of the signal, as well as the upper and lower frequency limit, depends on the selected station and are set forth in the input file.

The program can be tested for two correlated events recorded at the same station, HSPB. One larger event of magnitude M_L 3.2 is defined as master event, while a smaller event of magnitude M_L 2.0 is chosen as an EGF. The high correlation of 0.9 indicates similar source mechanism and location. As they are nearly collocated and observed at the same station, the responses from path, site and instrument will be the same and therefore cancels out. The EGF is at least one order of magnitude smaller than the master event and small enough to be considered a point source. The corner frequency of the EGF is assumed to be higher than for the master event, and therefore it will be outside the frequency range of interest and cannot be seen in the frequency spectra.

The method is applied in the frequency domain using S-phases. Spectral division of two identical waveforms results in a delta function and gives a flat spectra as the result of zero duration (Figure 3.6). In Figure 3.7 the EGF is deconvolved from the master event. The two seismograms in the upper right corner show the numerator and denominator which is the master event and the EGF, respectively. To the left is the spectral traces for each event, and below is the quotient spectrum obtained by dividing the numerator on the denominator. The spectral division is stabilised by applying a water-level of 10^{-6}, that will replace zeroes in the denominator with a fraction of the largest value. The source time function of the numerator is given in the lower right corner with the reconvolved signal above. The latter matches the seismogram of the larger event.

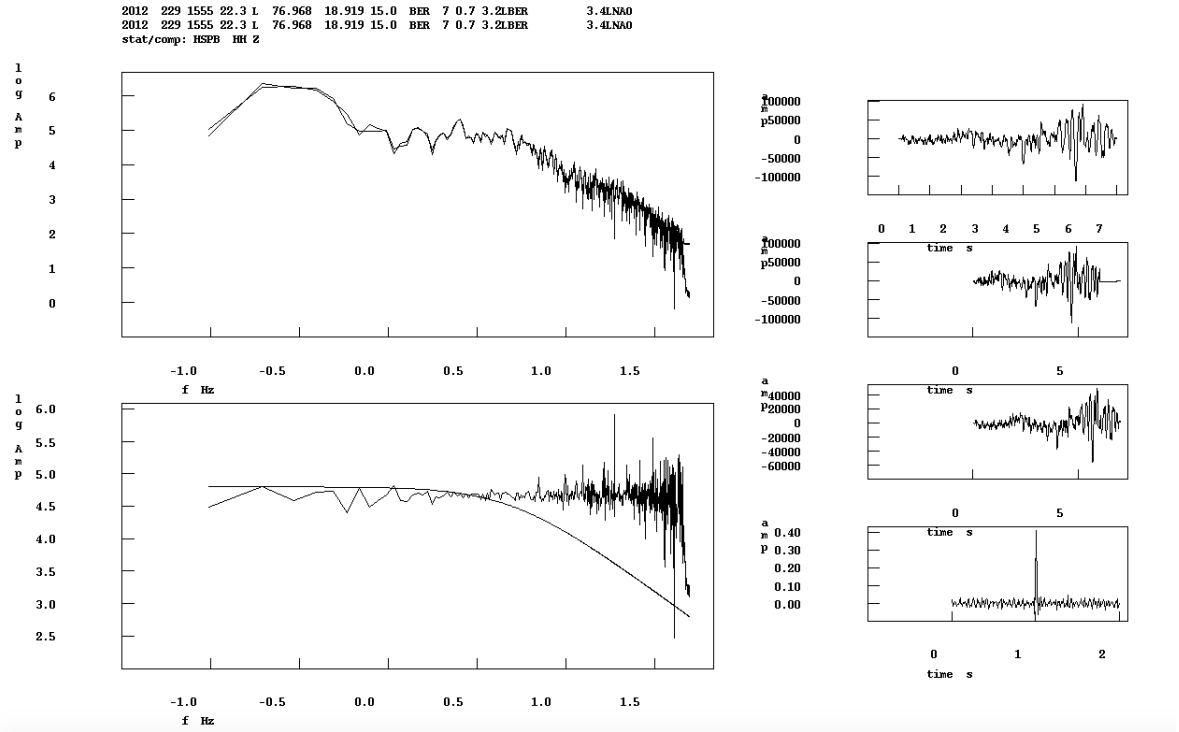

Figure 3.6: Deconvolving the seismogram of an event from itself gives one large spike as source time function.

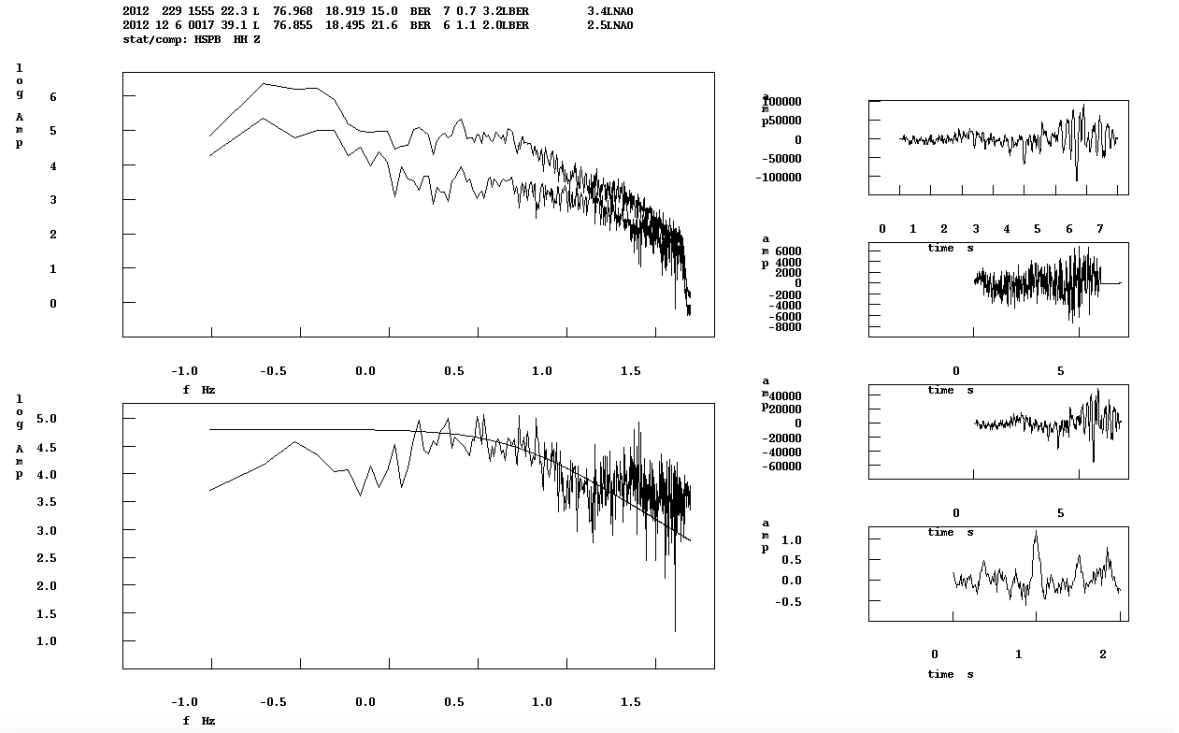

Figure 3.7: Deconvolving the seismogram of a smaller event, referred to as an EGF, from a larger master event, will remove instrument, travel path and site effects and give the source time function of the larger event. The computed spectrum line is adjusted according to the observed spectral shape.

3.5.4 Determination of source parameters

The final source time functions can be used for estimation of source parameters. Source duration will be measured and used to calculate corner frequency, f_c, stress drop, $\Delta\sigma$, and source radius. Seismic moment, M_0, will be derived from the flat part of the displacement spectra.

The source time duration is given by T and combines rupture and rise time. This value is measured as accurate as possible from the source time function and it will be converted into corner frequency, which is given as $2/T$ in the spectrum and related to frequency as $f_c = \frac{1}{\pi T}$ (Stein and Wysession, 2003).

Once the corner frequency is calculated, the source radius a can then be estimated for a circular fault as

$$a = 0.37v/f_c \tag{3.15}$$

where v is the velocity of either the P or S-wave and f_c is the corner frequency. (Havskov and Ottemöller, 2010). The value 0.37 is the κ_s factor for S-waves (Brune, 1970).

Seismic moment, M_0, is a direct measure of the size of an earthquake and the energy released. It depends on the fault area, S, the average amount of slip, $\bar{D}$, on the fault, and μ which controls the rigidity of the material affected by the fault. Seismic moment can be estimated from the amplitude spectra and with a precision of a factor of two (Stein and Wysession, 2003).

$$M_0 = \mu \bar{D} S \tag{3.16}$$

For a circular fault with radius a, the stress drop can be estimated as

$$\Delta\sigma = \frac{7}{16} \frac{M_0}{a^3} \tag{3.17}$$

Stress drop is defined by ratio of slip to fault dimension. Hence, a small uncertainty in source radius will cause a large error in stress drop. It can be determined within a factor of 2-3. Over time, stress accumulates along faults and when the fault slips, strain is released and the change in stress across a fault before and after rupture is the stress drop and can be estimated from the radiated seismic energy. Stress drop is important for the understanding of the earthquake physics. It is also important in modelling of ground motion attenuation as the stress drop will affect the resulting ground motion (Stein and Wysession, 2003).

4 Results

The first part of this chapter will present the results from the relocation process performed in hypoDD. Three different values of maximum hypocentral separation between events are used and with additional focus on the best solution. The second part includes the results of the water-level deconvolution and the estimation of source parameters.

4.1 HypoDD applied to the Storfjorden earthquake sequence

4.1.1 Catalogue data

A total of 2084 earthquakes in the Storfjorden area have been recorded at a minimum of four stations from early January 2007 until November 2016. The number of events that have at least four observations and selected into the preprocessing program *ph2dt* is 2072. P and S-phase data from the earthquake catalogue are then used to form travel time differences for earthquake pairs at common stations. In this study, travel time differences for event pairs with a separation distance of less than 5, 10 and 20 km, respectively, and at stations not more than 900 km away, are obtained during the preprocessing of the data in *ph2dt*. A strong neighbour is defined by a minimum of eight observations and each event allows a maximum of 30 neighbouring events. A minimum of four links and a maximum of 200 links are saved for each event pair. In addition, a minimum pick weight of 0 is allowed to make sure that all available phase pair are considered.

When the catalogue data is created it is difficult to obtain well-linked events. The average number of links for each event pair is five. That means that weakly linked events are also included (see Table 1). The MAXDIST, MINLNK, MINOBS and MAXSEP parameters are all critical for the linking of events. All parameters specified in the control file are held constant, except from the maximum hypocentral separation between event pairs (MAXSEP) which varies throughout the different runs of the program. The hypocentral distance allowed between events has a large effect on the forming of phase pairs, links to neighbouring events and clustering. During the preprocessing outliers with delay times larger than expected, are discarded. Input values to *ph2dt* is given in Appendix A and details from the program runs based on three different values of MAXSEP are given in Table 1.

MAXSEP (km)	P-phase pair selected	S-phase pair selected	Outliers	Weakly linked events	Linked event pairs	Average links per pair	Average offset (km) between linked events	Average offset (km) between strongly linked events
5	93,270 (78%)	81,000 (78%)	29,213 (13%)	2038 (98%)	31,349	5	3.694	3.746
10	507,856 (87%)	442,652 (88%)	59,809 (5%)	1697 (81%)	171,457	5	7.041	6.211
20	1,632 783 (90%)	1,389 324 (91%)	70,970 (2%)	1528 (73%)	559,412	5	12.562	8.374

Table 1: Results of program runs with varying values of MAXSEP.

4.1.2 Cross-correlation data

Waveform similarity is measured between all events by the cross-correlation function utilized in CORR, as mentioned in subsection (3.4.2). The program is run twice with a minimum correlation value of 0.8, a passband of 2-5 Hz, but with a different signal duration (Figure 4.1). For event pairs to be correlated a minimum number of two stations are required. Event pairs need to be located not farther than 20 km apart to calculate correlation. The maximum distance between event and station is 500 km. A selection of correlated earthquakes with a similarity of at least 0.95 are presented in Figure 4.2.

With the longest signal duration and a required correlation of at least 0.8, a total of 13,000 differential times are formed, where 4647 P and 8353 S cross-correlated differential times. Stable locations are obtained by a minimum distance cut off of 4 km and a residual cut off of six times the standard deviation. 40 percent of the cross-correlated data is relocated. Using a shorter signal results in 18,034 differential times. 5538 of these are cross-correlated P differential times, while 12,496 are S cross-correlated differential times. Half of the data (51 %) is removed during the iterations and reweighting. The best solution is obtained by using the longest signal duration and this will be used for the final relocations.

4.1.3 HypoDD relocations

After the absolute travel times from the earthquake catalogue and the differential travel times from cross-correlation have been formed for earthquake pairs, they are used as input to the hypoDD program to compute double-difference earthquake locations. The number of catalogue P and S differential times are considerably larger than for the differential times derived from cross-correlation, by an approximate factor of 100. Before combining the two data types, the relative quality between the two data types is determined by relocating each data type separately. This is also done to find the proper weights for each

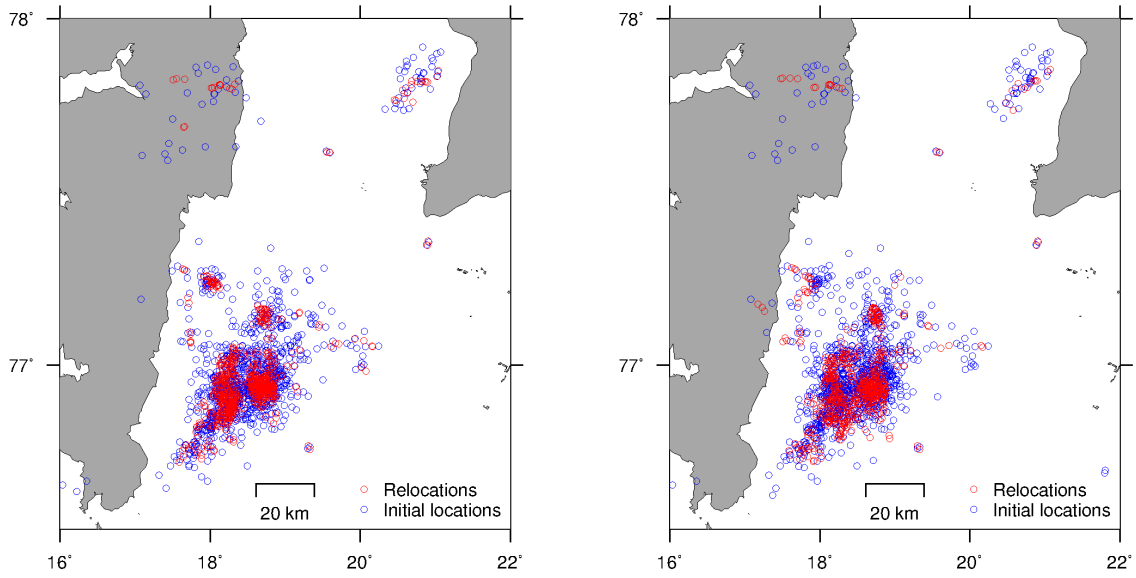

Figure 4.1: Relocated cross-correlation data with different signal duration. The left figure has twice as long duration as the right one, and is more constrained than the other.

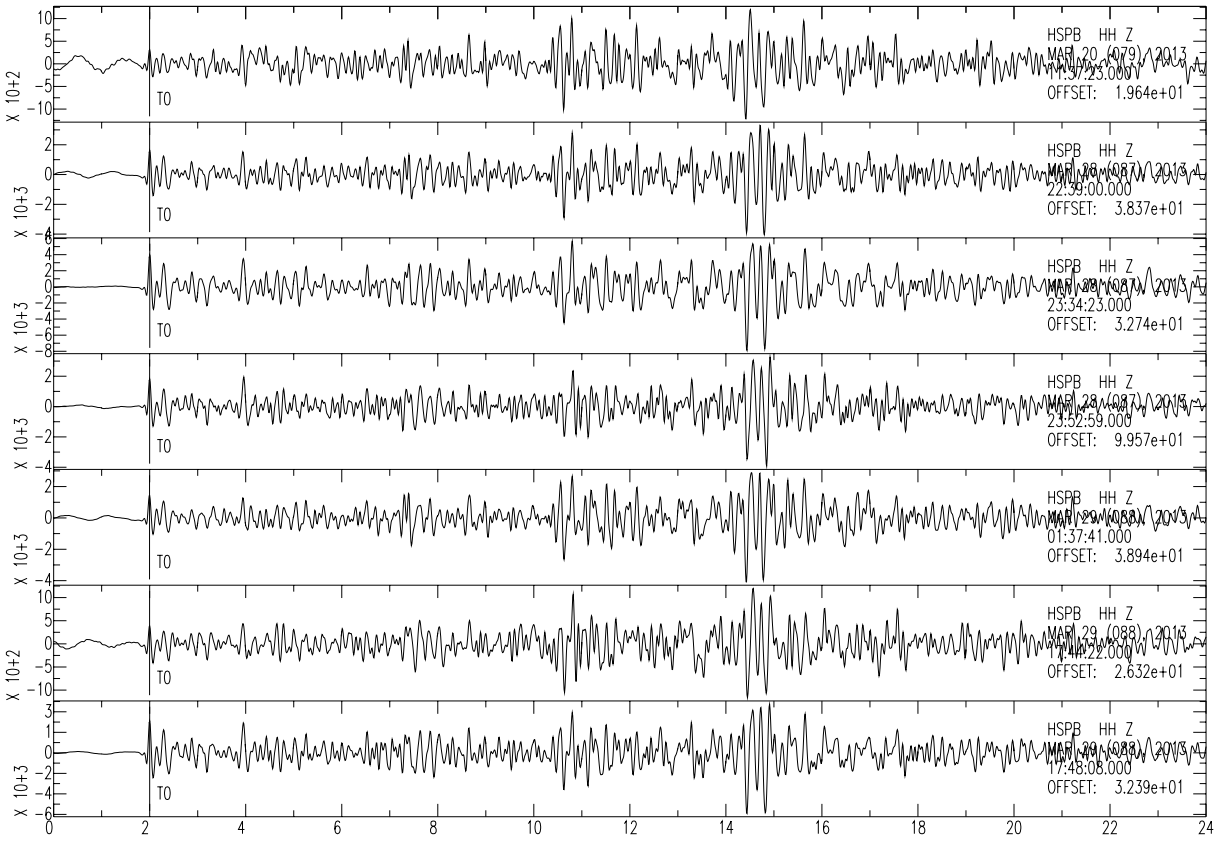

Figure 4.2: Demonstration of waveform similarity between seven earthquakes with a correlation coefficient of at least 0.95.

data type during the inversion.

In *hypoDD* events are grouped into clusters. To form a continuous cluster, a minimum of one cross-correlation and four catalogue links for each event pair are required. The starting locations are taken from the earthquake catalogue and the system of double-difference equations are solved in LSQR mode. Five sets of five iterations each are performed. Additional weighting is also applied during the inversion and the weighting scheme is given in Table 2. For the first two sets of iterations, the cross-correlation data is down-weighted with a weighting of 0.01 relative to the catalogue data, which are given a weight of 1.0 for P and 0.5 for S-phases. Additionally, the catalogue data is re-weighted according to misfit weight with residual cut off of ten times the standard deviation. For the next iterations, the residual threshold decrease and the separation distances between events continue to get smaller. Then, greater weights are given to the cross-correlation data, while the catalogue data is down-weighted. A residual cut off of four times the standard deviation and a distance threshold of four kilometres is set in order to let the cross-correlation data control the small separation distances.

All relocations done in *hypoDD* are based on a one-dimensional velocity model given in Table 3 and shown in Figure 4.3. The model is the standard velocity model for Norway, developed by Havskov and Bungum (1987), with additional layers to obtain a more gradual velocity increase with depth. It consists of twelve layers and considers a constant v_p/v_s ratio of 1.73. The model was developed for western Norway.

	Cross correlation data				Catalogue data			
Iterations	A priori, P-wave WTCCP	A priori, S-wave WTCCS	Misfit weight WRCC	Distance weight (km) WDCC	A priori, P-wave WTCTP	A priori, S-wave WTCTS	Misfit weight WRCT	Distance weight (km) WDCT
1-5	0.01	0.01	-9	-9	1.0	0.5	10	-9
6-10	0.01	0.01	-9	-9	1.0	0.5	8	5
11-15	1.0	0.5	-9	-9	1.0	0.5	8	5
16-20	1.0	0.5	6	4	0.1	0.05	6	4
21-25	1.0	0.5	6	4	0.01	0.005	6	4

Table 2: Weighting scheme used in the inversion.

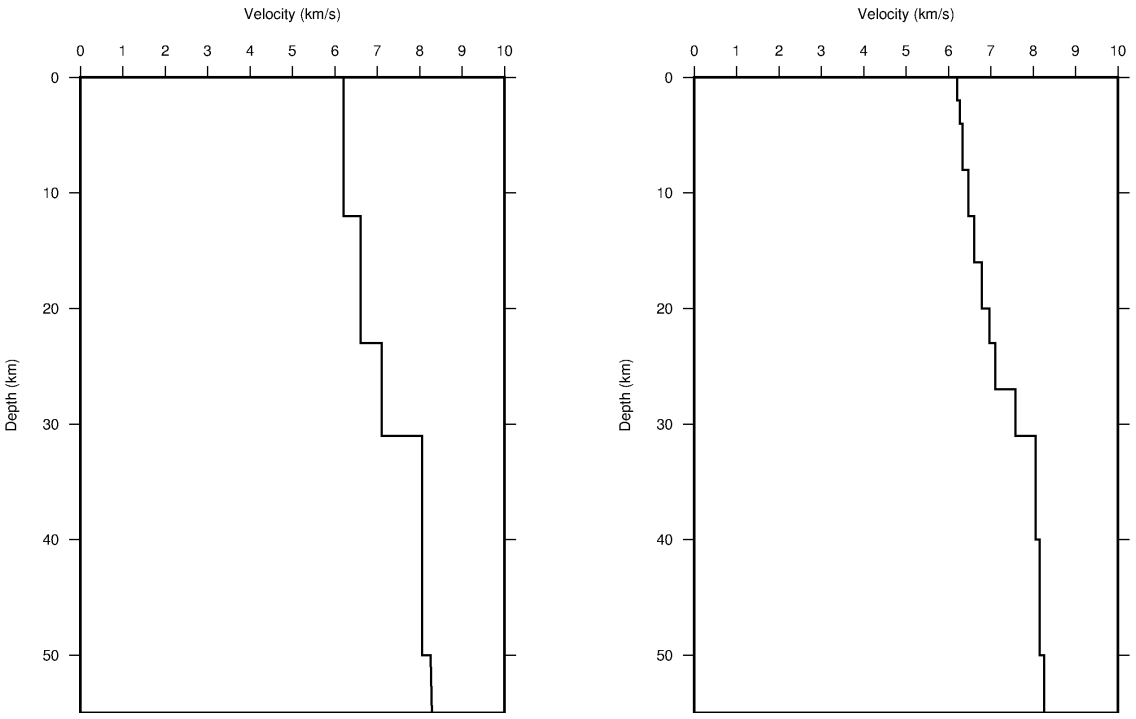

Figure 4.3: One-dimensional P-wave velocity models: (a) The standard velocity model for Norway by Havskov and Bungum (1987). (b) The original velocity model with additional layers used in this study for the double-difference relocation.

Depth of layer (km)	Layer velocities (km/s)
0.0 - 2.0	6.20
2.0 - 4.0	6.27
4.0 - 8.0	6.33
8.0 - 12.0	6.47
12.0 - 16.0	6.60
16.0 - 20.0	6.78
20.0 - 23.0	6.96
23.0 - 27.0	7.10
27.0 - 31.0	7.58
31.0 - 40.0	8.05
40.0 - 50.0	8.15
50.0 -	8.25

Table 3: Velocity model used in *hypoDD*.

Relocation with MAXSEP 20 km

To begin with a maximum hypocentral distance of 20 km between event pairs are allowed when forming travel-time differences. It gives a total number of 2070 events after differential time match, in which 2016 events are distributed over two clusters, while the remaining 54 events are isolated events. Cluster #1 has 1991 events and cluster #2 has 25 events. Hence, a significant number of the total number of events are kept for the relocation.

For the first ten iterations, the hypocentral values are highly fluctuating. An ill-conditioned system of double-difference equations are indicated by the condition numbers which remains high (> 150) even with a high damping factor of 200 and 150. For the next iterations, misfit and distance weights are applied. The data becomes more constrained and the resulting condition number ranges from 40-80 with damping values of 70 and 60. As the condition of the system improves, the solution is converging. The mean absolute change in horizontal direction (DX) decrease from 2726 m to 24 m. In vertical direction (DY), 3793 m converge down to 29 m. Depth (DZ) changes from 4912 m to 44 m, while origin time (DT) go from 482 ms to 3 ms. The catalogue RMS residual changes from 562 ms to 180 ms, while the cross-correlation RMS residual changes from 842 ms to 4 ms.

The final result is given in Figure 4.4 and relocated events for each year from 2008 through 2016 are shown in Figure 4.5. A MAXSEP value of 20 km includes a great deal of data, but through an iterative procedure with weighting and re-weighting of data, the number of relocated events is 1035. The more diffuse initial locations are gathered into clusters, in which some of them are showing a clear NE-SW trend. One large cluster is formed and there is a chance that events belonging to an area of different velocity structure is included. Therefore, a more stable solution might be achieved by selecting a smaller MAXSEP value, preferably without excluding too many events.

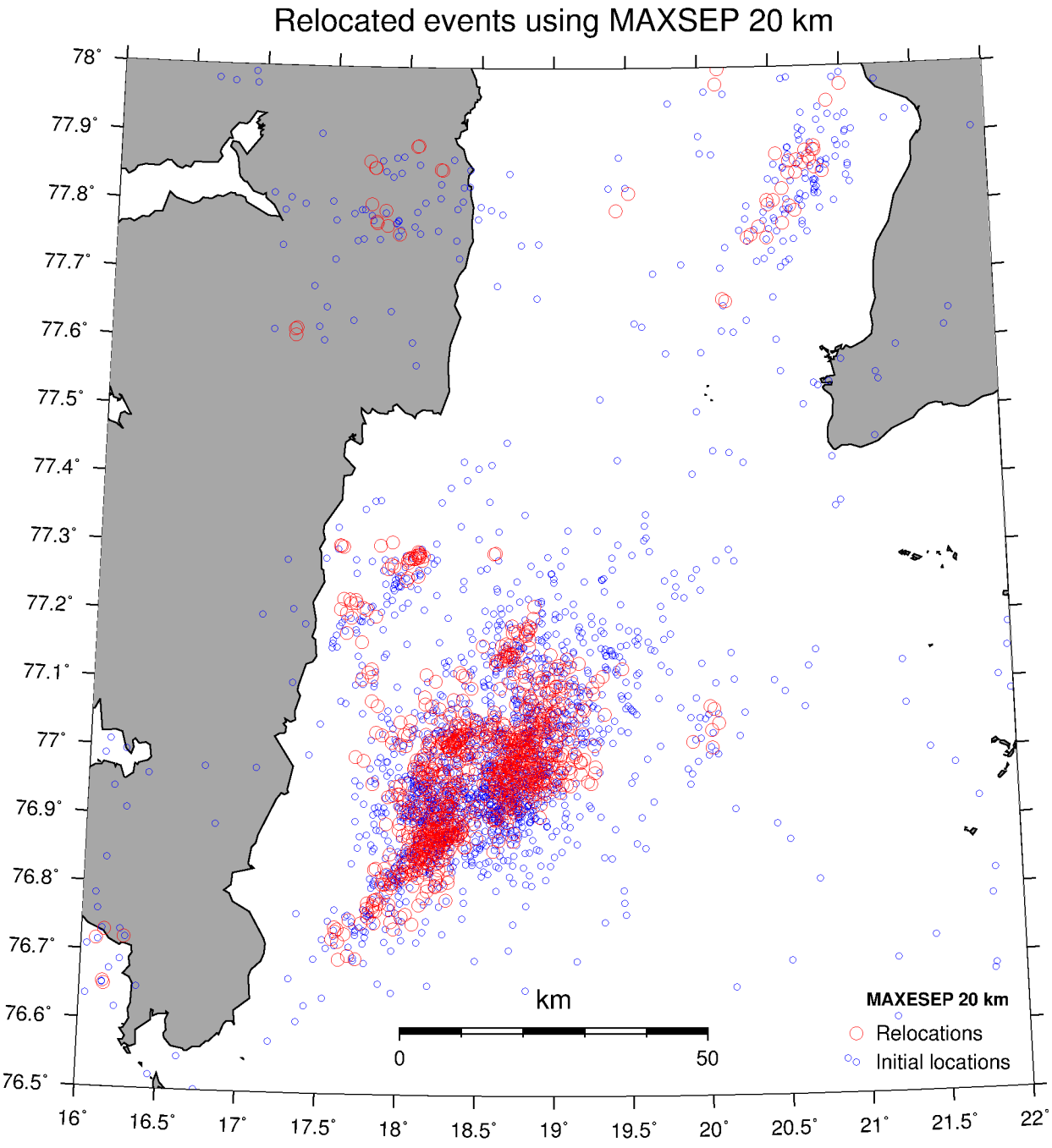

Figure 4.4: Double-difference relocations using a maximum hypocentral separation of 20 km between event pairs. Blue circles are initial locations and red circles are relocations.

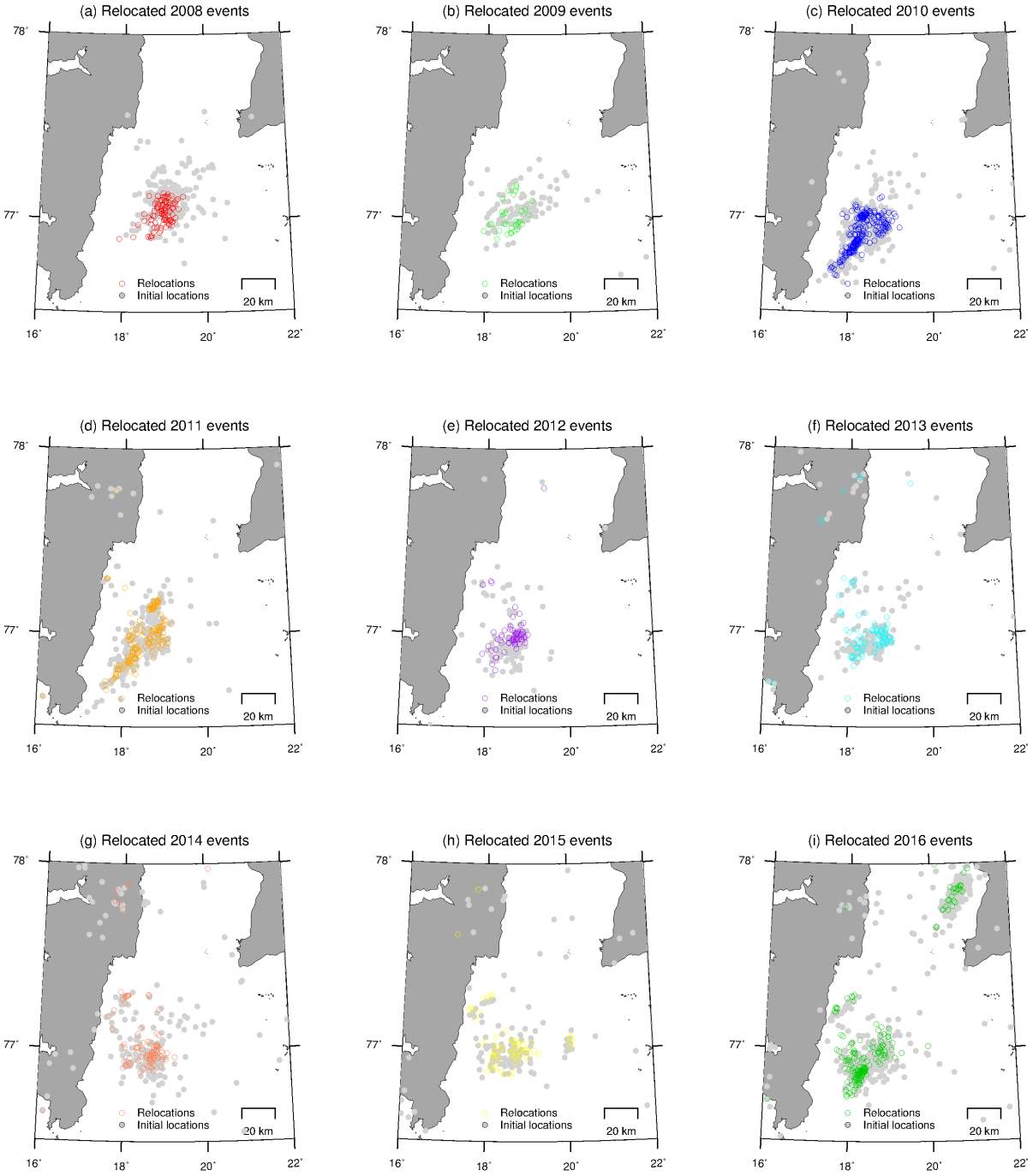

Figure 4.5: Double-difference relocations using a maximum hypocentral separation of 20 km between event pairs. Filled, grey circles are initial locations and open circles are relocated events with different colour for each year.

Relocation with MAXSEP 10 km

A hypocentral separation of less than 10 km between event pairs results in 2033 selected events after differential time match. 1956 of these are clustered events, while the number of isolated events are 77. The number of clusters has increased to 23, where the majority of events are distributed over three clusters. Cluster #1 has 1723 events, cluster #2 has 98 events, whereas cluster #3 contains 60 events. Cluster four and five have 14 and 12 events, respectively, while the number of events for the remaining clusters are five events or less. Clusters of three or two events are not successfully relocated.

As for a MAXSEP value of 20 km, the system still appears unstable for the first two sets of iterations. High damping can to some extent regularise the condition of the system and the fluctuating values seen for MAXSEP 20 km are not present. Instead, the values are slowly converging. The following three sets of iterations results in more appropriate condition numbers varying between 40 and 80 with damping values between 70 and 50. The average absolute value of horizontal shift (DX) is starting at 2407 m and decrease to 25 m at final iteration. The shift in north-south direction (DY) changes from 2940 m to 31 m, and the average absolute value of the change in depth (DZ) changes from 3447 m to 46 m. The origin time (DT) is changing from 386 ms to 3 ms. The catalogue RMS residual decreases from 557 ms to 201 ms and the cross-correlation RMS residual decrease from 821 ms to 3 ms.

The result from the relocation of all clusters is shown in Figure 4.6 and Figure 4.7. Again, the relocations represent a useful improvement of the initial locations. A MAXSEP of 10 km results in the relocation of 988 events. It is a small decrease from the previous relocation attempt. However, the same features appear on the map, some even more defined. The smaller event distance separates the largest main cluster from the smaller cluster to the north-east. More events are included in this cluster. With a hypocentral distance of not more than 10 km, there is an overall improvement. Though, it should still be possible to make further improvements using more restrictive values.

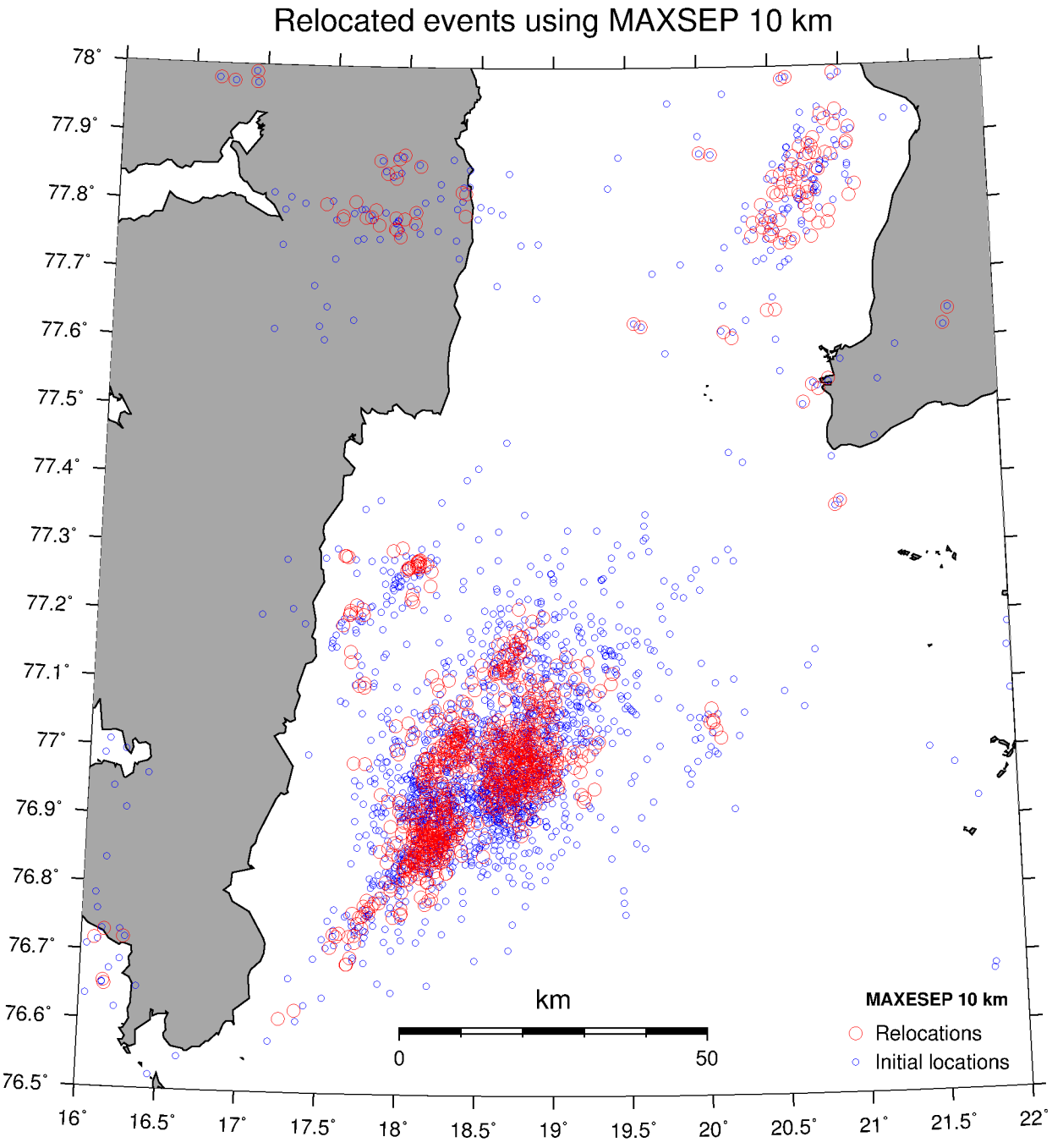

Figure 4.6: Double-difference relocations using a maximum hypocentral separation of 10 km between event pairs. Blue circles are initial locations and red circles are relocations.

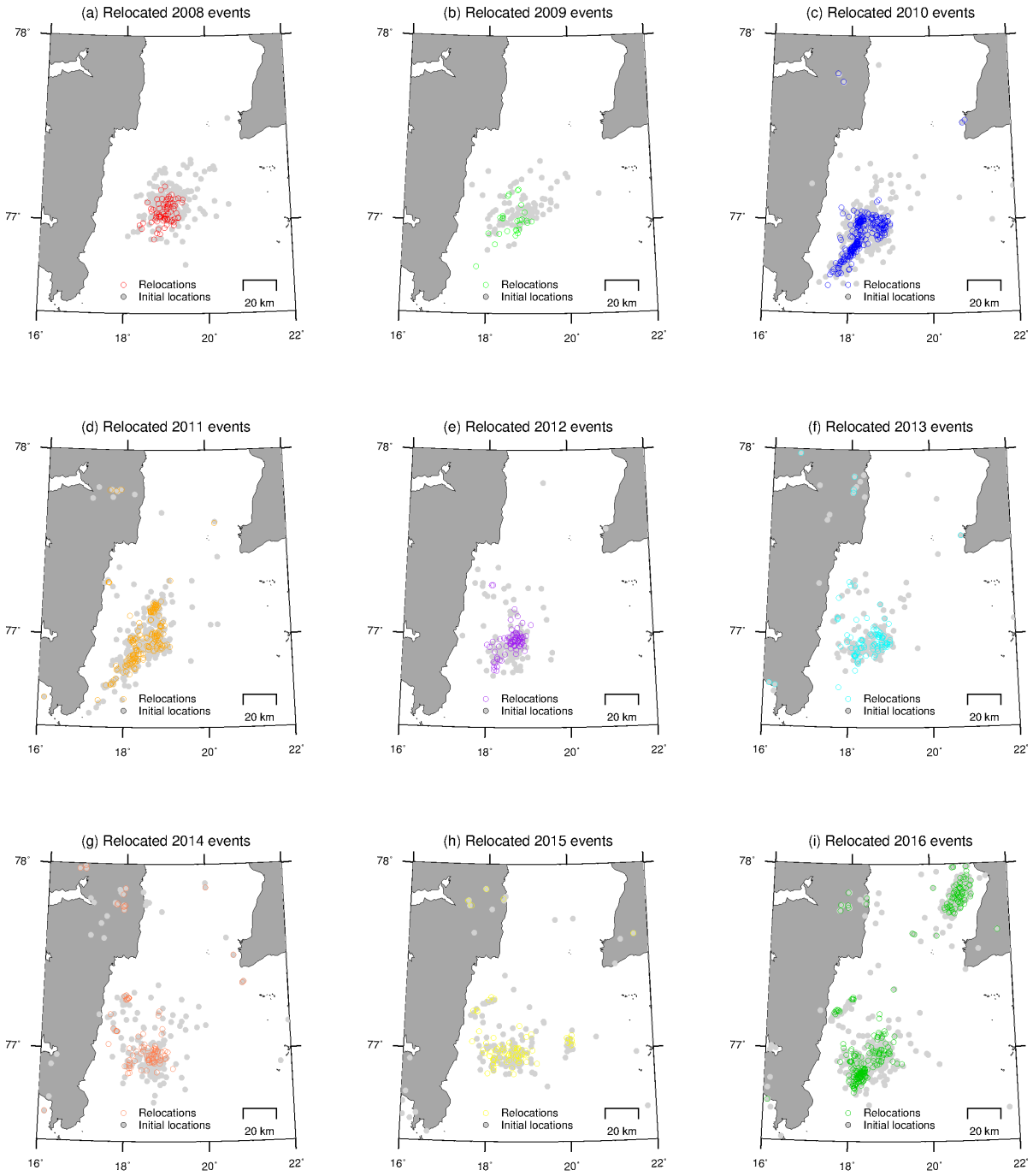

Figure 4.7: Double-difference relocations using a maximum hypocentral separation of 10 km between event pairs. Filled, grey circles are initial locations and open circles are relocated events with different colour for each year.

Relocation with MAXSEP 5 km

In the hope of finding a more stable solution and still keep enough events to achieve a representative image of the seismicity, a more stringent value of 5 km is chosen for the maximum event separation. After differential time match, there are 1916 events. 1763 are clustered events, while 153 are isolated events. A total of 50 clusters are formed, but more than half have three events or less. The largest cluster includes 1542 events, while cluster #2 to the north-east contain 68 events. Cluster #3 through cluster #12 contains 16 to four events.

The largest cluster is relocated using damping values of 100, 80, 60 and 50 and yield condition numbers between 95 and 40. The largest change in the hypocentral parameters are seen for the first set of iterations. The solution stabilises faster than for larger MAXSEP values. The RMS residual for catalogue data converges from 463 ms to 204 ms, while for the cross-correlation it starts at 739 ms and decrease down to 4 ms. From the very first to the final iteration, the average absolute shift in hypocenter location and origin time is changing from 1569 m (DX), 2245 (DY), 2881 (DZ) and 250 (DT) to 21 m, 26 m, 37 m and 3 ms, respectively.

All clusters are relocated and the final results for using a MAXSEP of 5 km is given in Figure 4.8 and relocated events for each year of the sequence is shown in Figure 4.9. After the relocation process, 894 events are located. The selected events are mainly those that occur in the most active parts of the area, and it seems like this value is too small and does not allow for enough linking between events.

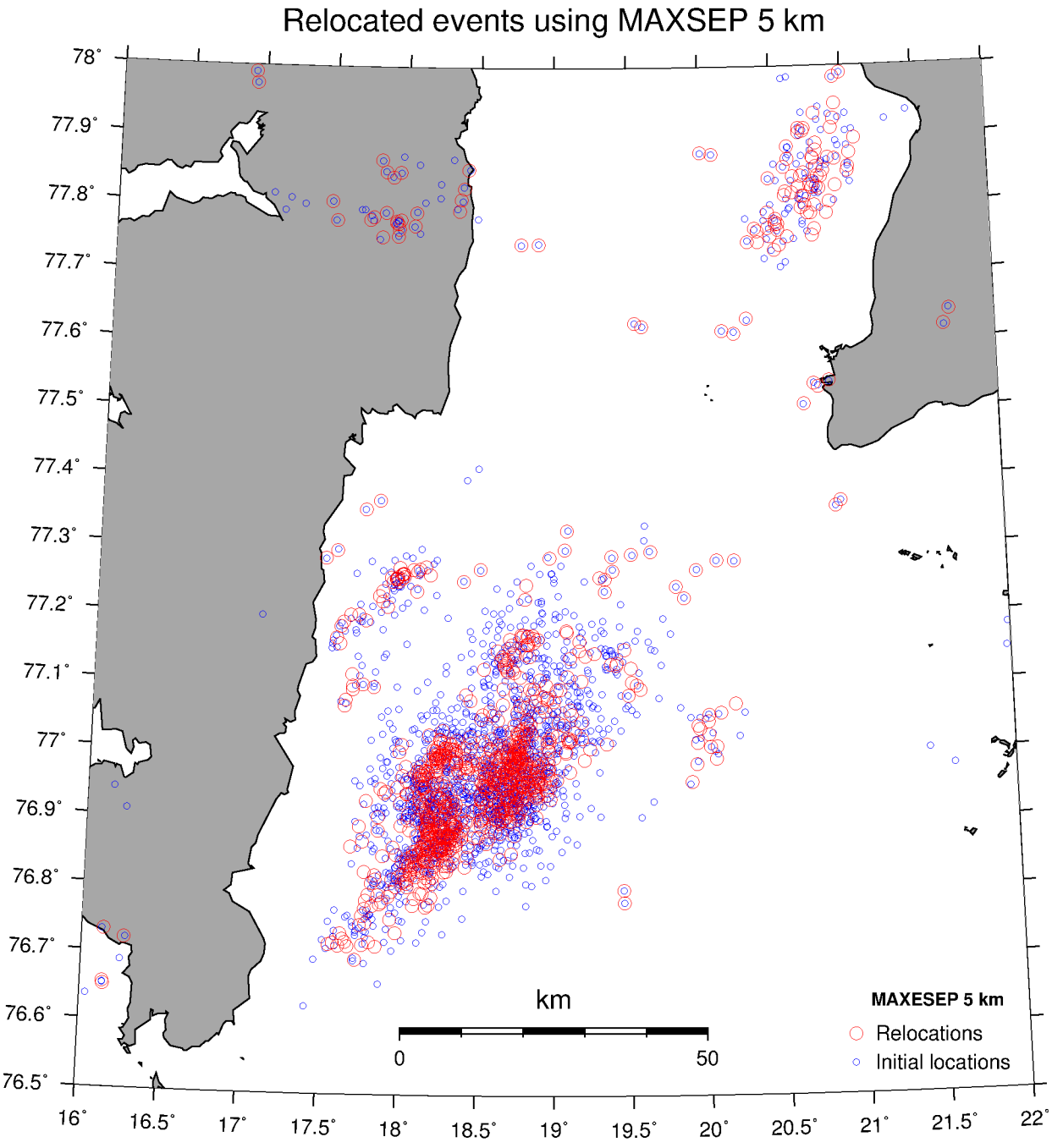

Figure 4.8: Double-difference relocations using a maximum hypocentral separation of 5 km between event pairs. Blue circles are initial locations and red circles are relocations.

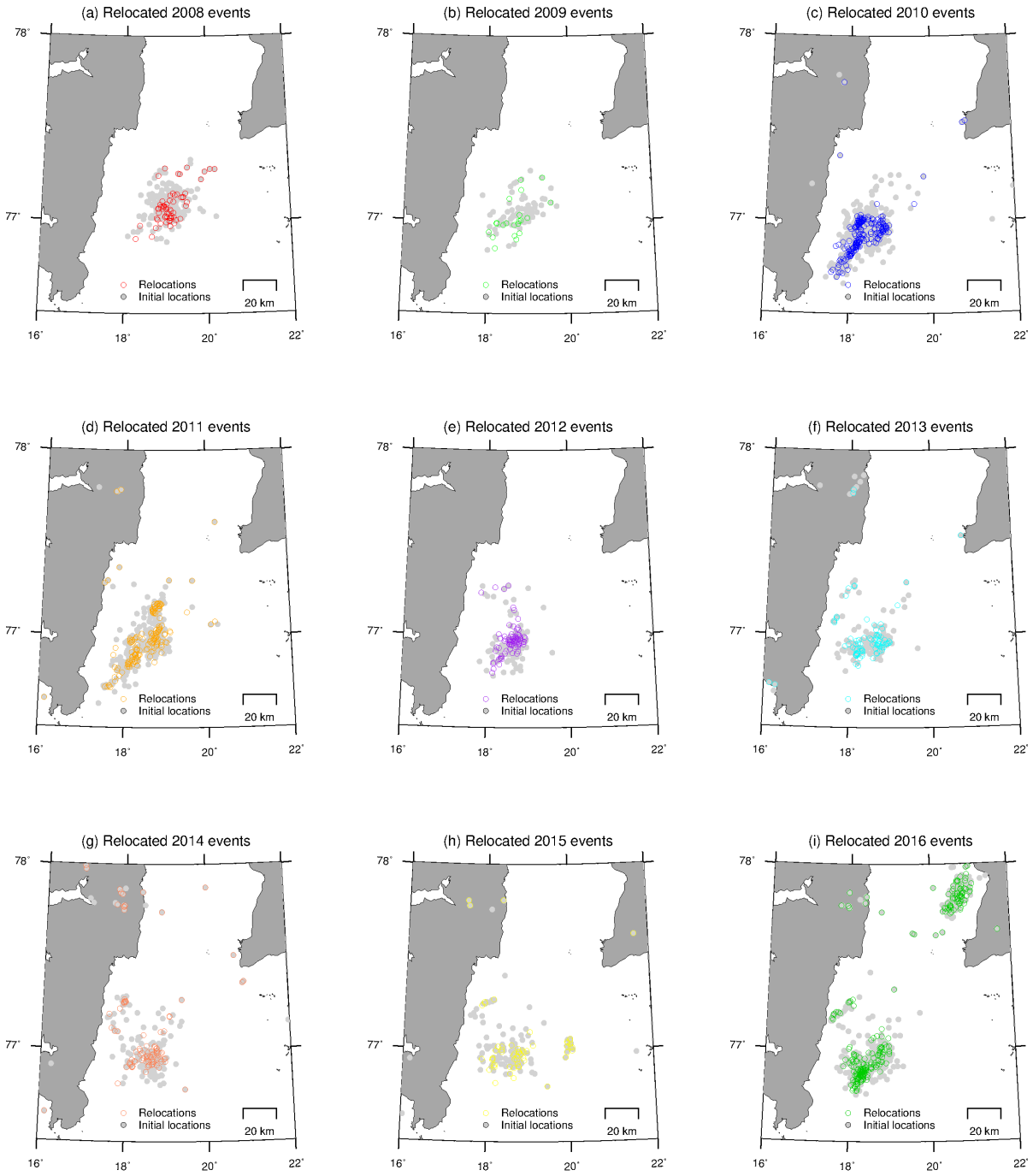

Figure 4.9: Double-difference relocations using a maximum hypocentral separation of 5 km between event pairs. Filled, grey circles are initial locations and open circles are relocated events with different colour for each year.

4.1.4 General overview of results

The double-difference algorithm clearly manages to improve the relative locations for all values of MAXSEP and a few general observations can be made. The more diffuse seismicity has collapsed into several clusters, in which some are showing clear linear trends. The most prominent features are at least four linear structures located in the largest cluster. In addition, there are indications of a parallel and linear structure both to the west and to the north of the largest cluster. Further discussion of these will be made in the next chapter.

The year-by-year plot shows the spatial and temporal distribution of the sequence from 2008 until 2016. The main event of magnitude $M_W = 6.1$ on 21 February 2008 marks the beginning of the sequence and the subsequent activity is mainly concentrated around the epicenter of the main event. Then, a southwestern extension of the sequence remains active for at least two years (Figure 4.7c-d). Later, more diffuse seismicity occurs in the central area and to the north and northwest of this region, but some clustering is also observed (Figure 4.7e-h). At last, following the magnitude $M_W = 5.3$ event on 29 March 2016, a seismic zone to the north-east initiates. In addition, some reactivation to the south-west and increased activity is evident from the results (Figure 4.7i).

The number of events and clustering of these, is strongly affected by the choice of maximum hypocentral separation between event pairs. A maximum event separation of 20 km is the least stringent criteria to forming of event pairs, neighbours and clusters, and results in one large cluster containing almost all the events. In comparison, the much smaller maximum event separation of 5 km results in far more clusters and the smallest number of clustered events. A value of maximum 10 km between event pairs manage to include a significant amount of the hypocenters, and at the same time give a reasonable clustering of events. With this in mind, I focus attention on the relocation results using a maximum hypocentral separation of 10 km.

4.1.5 Closer study of MAXSEP 10 km

The NE-SW structures that are resolved using the double-difference relocation might indicate the direction of actual faults. Based on the relocations and fault plane solutions, cross-sections are made both across and along the apparent seismicity trend (Figure 4.10). However, considering the structural complexity in this region and available fault plane

solutions, it is likely that it exist faults of other directions.

For the southwestern extension of the sequence, a NE-SW trend has been interpreted based on the relocation. However, fault plane solutions are indicating the presence of NW-SE structures as well. Presuming a NW-SE trending fault, profile A-A' and B-B' in Figure 4.11 indicate south-west dipping structures (Fig. 4.11b). The same dip is also seen in profile D-D' and F-F' in the same figure.

There are only few events in the cluster to the northwest, but it is possible that it follow the same NE-SW trend. In the profiles G-G' and H-H' in Figure 4.12, the hypocenters does not show any dip direction. Within the largest cluster there is no obvious trend, but some events in profile I-I', seem to be organised in a dipping plane towards south-east. The profile along the trend, J-J', show that the activity in 2016 makes the north-eastern extension of this cluster. In the north-east, the relocated events from 2016 seem to be organised in a NE-SW direction, but with some scatter. The profile made across this trend, K-K', and along L-L', reveals that the hypocenters are mainly occurring at a depth between 10 and 20 km. The uppermost part seems to be vertical, but with a small branch slightly towards south-east. The largest aftershock of the M_w 5.2 event is wrongly locating at the surface.

Overall, it seems to be an apparent dip towards south-east and south-west in different parts of the cluster, which can imply different directions of faults and mechanism. The earthquakes occur mainly at a depth between 10-25 km.

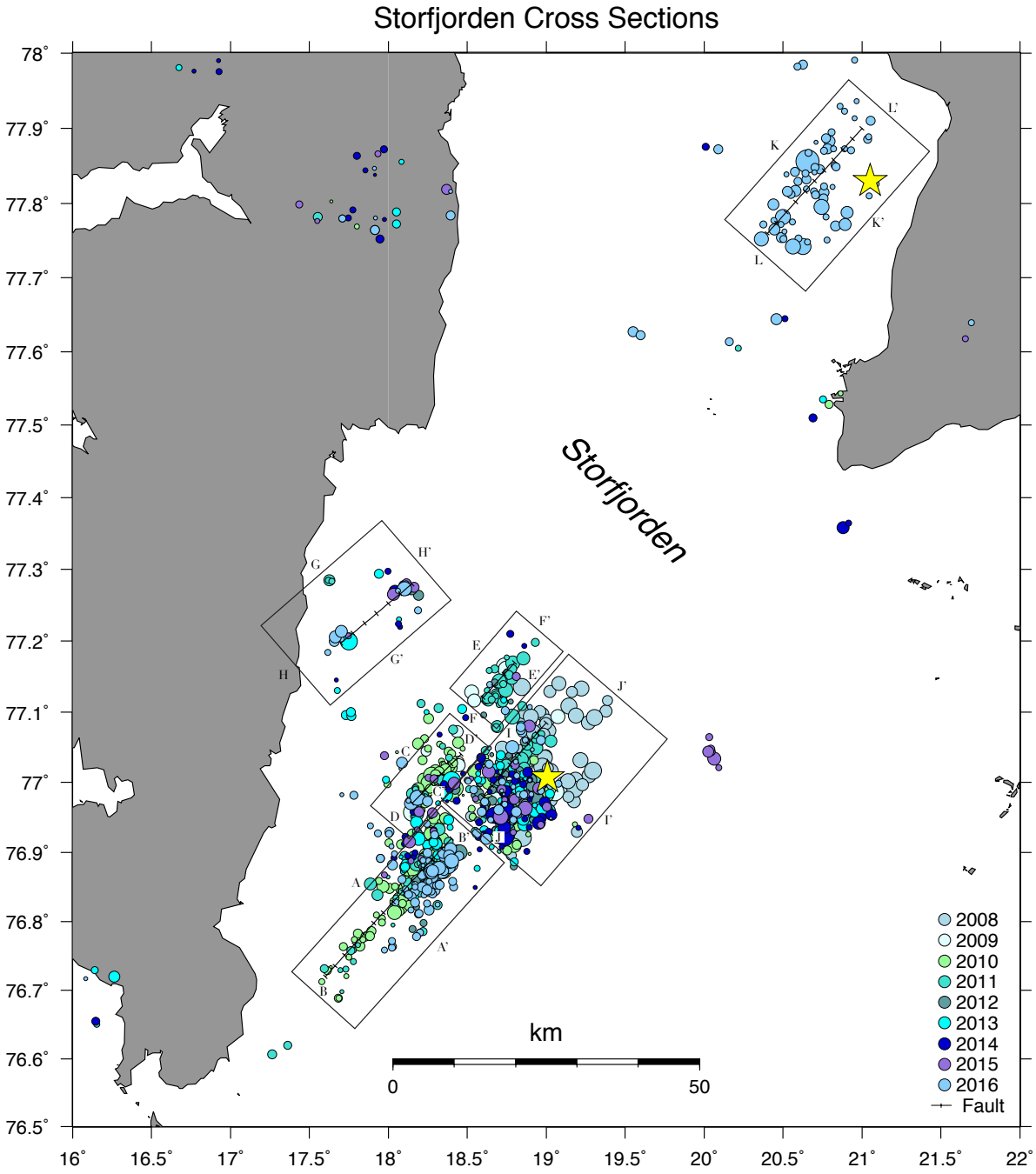

Figure 4.10: Relocated events are scaled by magnitude and given different colours depending on the year of occurrence. The two main events of magnitude 6.1 and 5.2 are indicated by the stars in the main cluster and in the north-eastern cluster, respectively. Linear structures, interpreted as faults, are also indicated on the map.

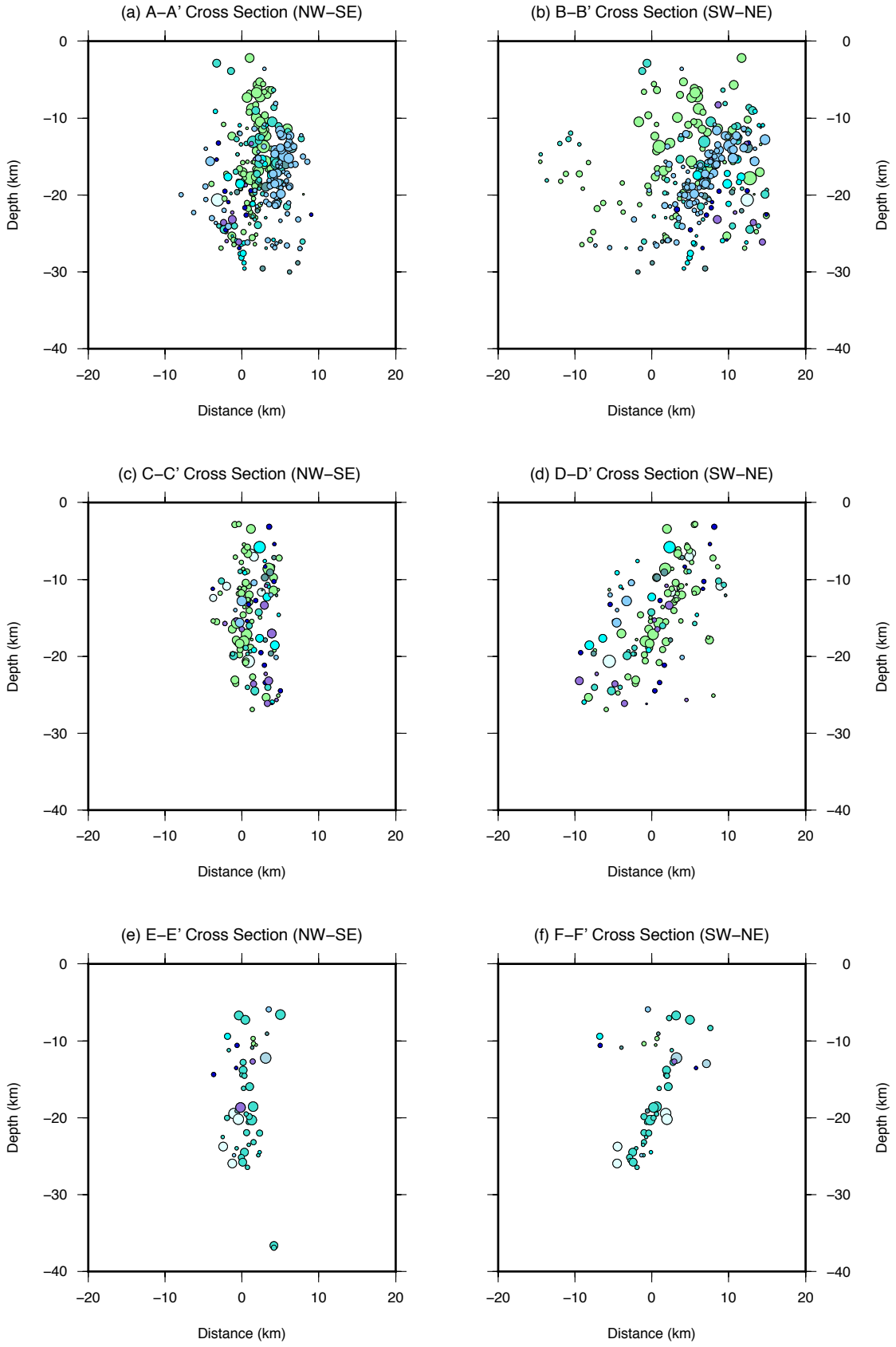

Figure 4.11: The figure shows cross-sections made across and along the apparent NE-SW seismicity trend. Width and length of each profile are shown in Figure 4.10.

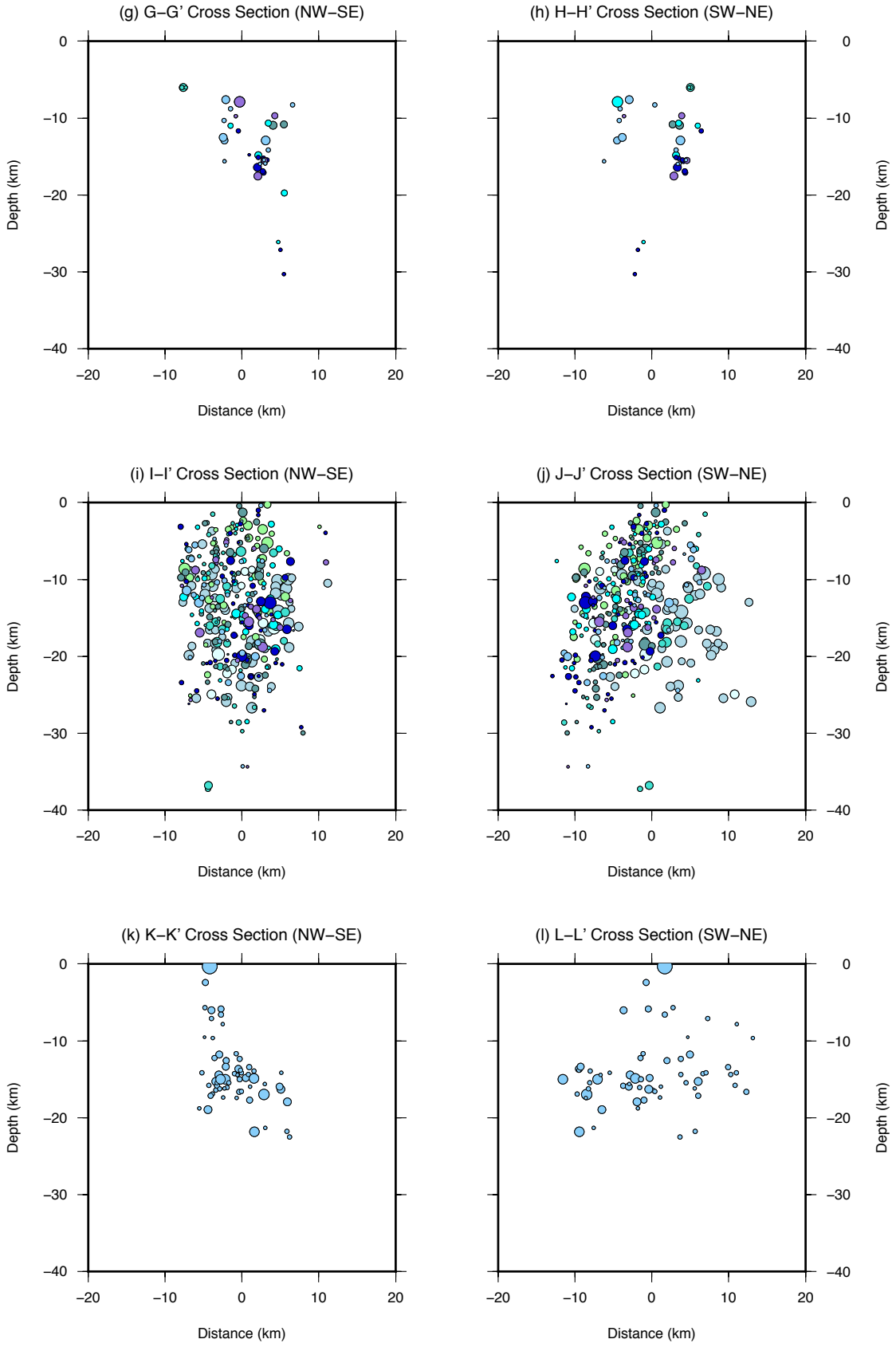

Figure 4.12: The figure shows cross-sections made across and along the apparent NE-SW seismicity trend. Width and length of each profile are shown in Figure 4.10.

4.2 Source parameters for Storfjorden earthquakes

4.2.1 Clustering of correlated events

The cluster analysis is accomplished using the XCLUST program as explained in subsection (3.5.1). The program is run by requiring a minimum correlation of 0.9 for event pairs to be included, and recordings from a minimum of three stations. In addition, a minimum number of six events has to be present in order to define a group. A total of 217 events are included and distributed over 20 clusters, ranging in size from 6-33 events. Waveform similarity is a good starting point for finding suitable empirical Green's function (EGF) earthquakes, as it will fulfil the criteria of very close location and nearly the same focal mechanism for the master event and the smaller event used as EGF. If they are located close to one another, the deconvolution will remove propagation and site effects from the earthquake of interest (Hutchings and Viegas, 2012). The correlated events are also located using the previously described double-difference relocation technique (section 3.3) and the improved locations for selected clusters are displayed in Figure 4.13.

4.2.2 Empirical Green's function analysis

For the 20 clusters that are found in XCLUST, I chose at least one event as a master event and then look for suitable EGF events for every cluster. As it should be at least one order of magnitude difference between the master event and the EGF, it is not possible to include all the events. In fact, for some clusters, a suitable master event or EGF is not always be available, limiting the number of events.

For the remaining clusters the water-level deconvolution can be performed in DECON (see subsection 3.5.3). A water-level of 10^{-6} is found to be an appropriate value as it reduces deconvolution instability and still preserve the original shape of the source pulse. Increasing the water-level will increase the smoothing of the resulting source time function, and eventually it will distort the source time function with the result of a re-convolved signal that differs from the original signal. Another parameter that affects the resolution of the deconvolved signal is the low-pass Gaussian filter. For the range of magnitudes in this collection of earthquakes, an alpha value of 100 is selected which means least possible filtering. The Gaussian remove noise, but one needs to be careful to not remove important features in the source pulse. A bandwidth with an upper frequency limit of 50 Hz and

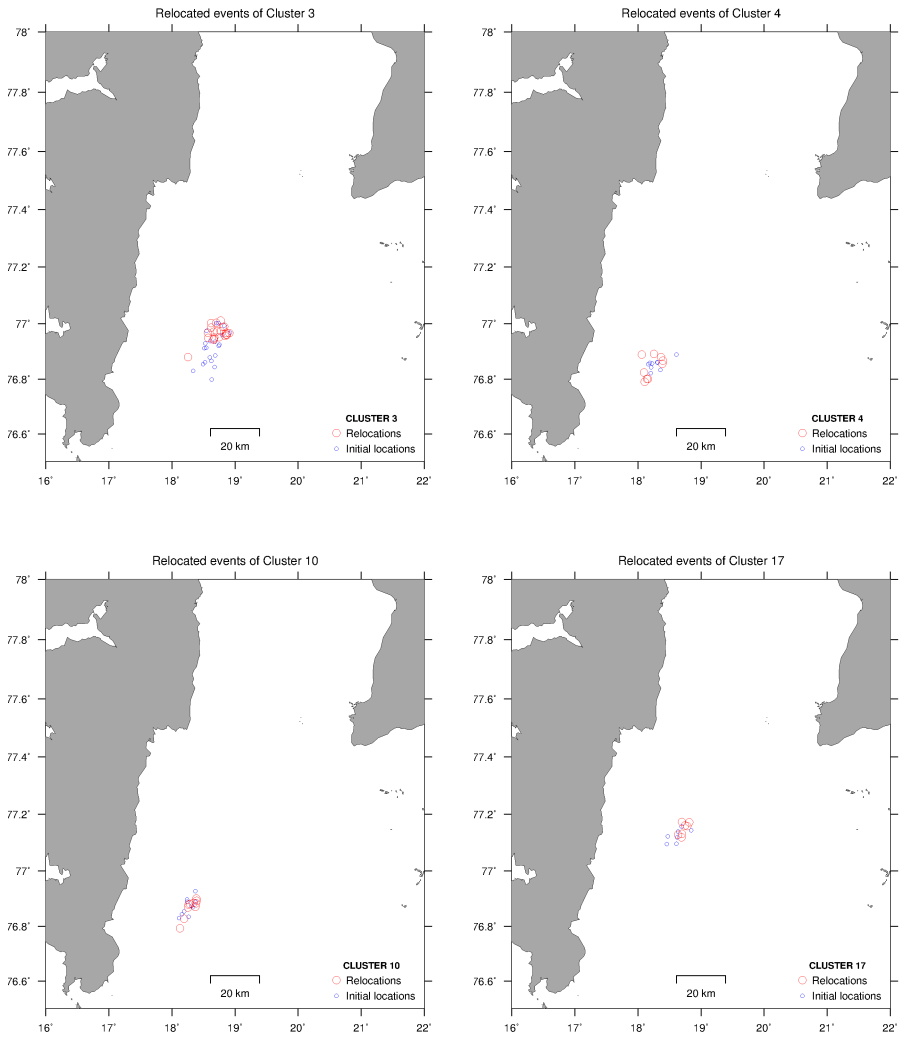

Figure 4.13: Relocations of correlated events from selected clusters. These clusters also give the most useful results in the EGF analysis.

lower limit of 1 Hz is selected, in which both earthquakes can be recorded with a good signal-to-noise ratio.

Initially, the search for S-phases is done for the seismic station HSPB, located in Hornsund in southern Spitsbergen. This is the station located closest to the Storfjorden earthquakes and reasonable results can be achieved by using its seismic records. However, azimuthal variations in the deconvolved source time functions should also be taken into consideration. In addition to HSPB, the stations at Kings Bay (KBS), Hopen (HOPEN) and Spitsbergen (SPA0), respectively, give only a few useful results, mainly from HOPEN. Making it difficult to account for directivity effects.

4.2.3 Source time functions

Cluster #3 is one of the clusters that has earthquakes which can be used in the EGF analysis. An overview of source parameters for the earthquakes in this cluster are given in Table 4. From Figure 4.13 it is obvious that the majority of relocated events are closely located. Within this cluster, I can identify three master events (M_L 2.3 to 3.2). For each master event, smaller events are chosen as empirical Green's functions. The EGFs are at least one magnitude smaller than the master event (M_L 0.9 to 2.0). The path, site and instrument effects are removed from the seismogram of the master event by dividing its spectra with the spectra of the EGF. The corner frequency of the smaller events is assumed to be outside the frequency bandwidth of interest, such that it is the source time function of the master event that is obtained.

The apparent source time function of the 3.2 magnitude event occurring on 29 February 2012 and recorded at HSPB, can be seen in Figure 4.14. Nine events within the same cluster are used as EGFs and deconvolved with the master event. The source time functions do not differ too much from one another. I assume triangular shape and measure the duration for each pulse and then use the average value to estimate the corner frequency. The onset can be estimated with confidence for most of them, but in cases where it is not crossing the horizontal line, an approximate measure can be made using the change in gradient.

For a second master event, six smaller earthquakes can be used as EGFs (Figure 4.15). The event occurred on 8 April 2012 and given a magnitude of 2.7. Compared to the source time functions for the first event, asperities introduce some ambiguity in the source time functions obtained for this event, which makes it more difficult to make precise measurements. For this event it was possible to compare with HOPEN station, which is located further away in the opposite direction. Eight events can be used as EGFs and produce a shorter source time function with a more clear and consistent shape.

Then, for a third master event of magnitude 2.3, recorded on 6 December 2012 on HSPB, five deconvolved traces are obtained (Figure 4.16). They all have quite similar shape and, as expected, the estimated duration is smaller than for the previous events. Unfortunately, no comparison with any of the other stations can be done.

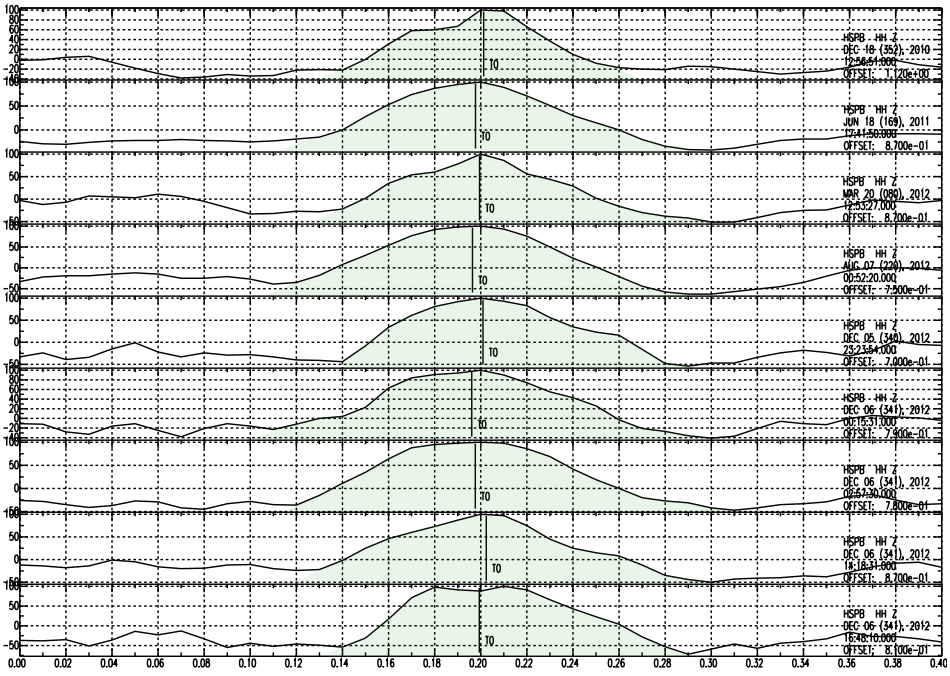

Figure 4.14: The source time function of the earthquake occurring on 29 February 2012 at 15:55 with a magnitude of 3.2 has an average source duration of 0.18 seconds. For demonstration purposes, the deconvolved waveforms are aligned at their peaks and also normalized according to maximum amplitude. Duration is measured within shaded area.

4.2.4 Earthquake source properties and scaling relationships

S-waves are used to determine source parameters for a compilation of ten earthquakes located in Storfjorden. The estimated parameters are source duration (T), corner frequency (f_c), source radius (a), stress drop (σ) and seismic moment (M_0). The result for all earthquakes is given in Table 4. From the total amount of correlated events, there is only a small portion which can be used. The other events are left out, either because they did not satisfy the criteria for EGF analysis, no S-phase could be found, or if the estimated source parameters appears unreasonable. It seems that for earthquakes with a magnitude of less than $M_L = 2.3$, unlikely small stress drop values ($\Delta\sigma < 0.1$ bar) are obtained. In general, the calculated corner frequencies are smaller than expected, and for these smaller events this makes an overestimation of source radius. In combination with low seismic moment, this give rise to very small stress drop values. Also, a high degree of asperities in the source time function is not optimal for source parameter estimation, as it is already made with large uncertainty.

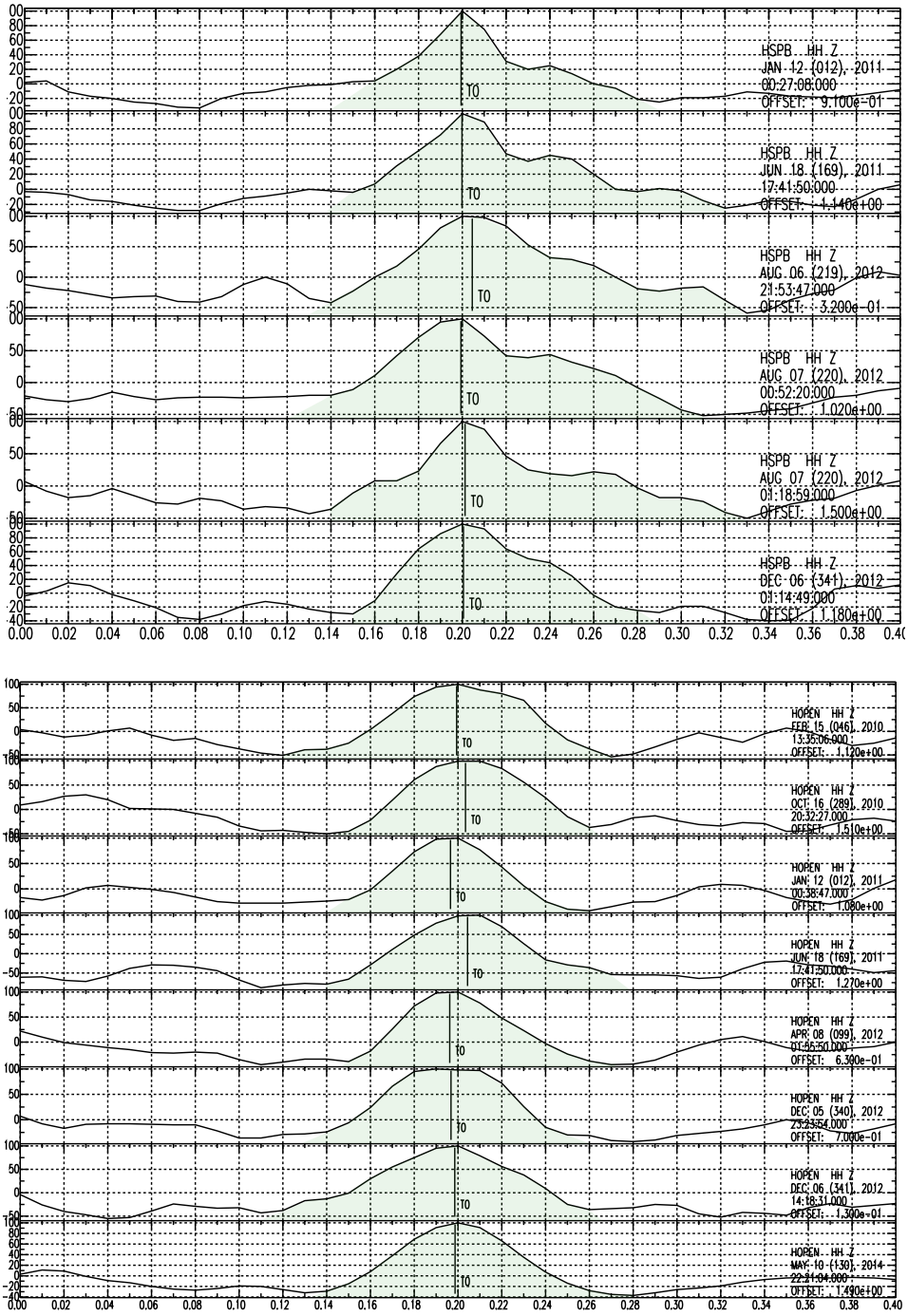

Figure 4.15: The source time function of the event on 8 April 2012 occurring at 01:35 with a magnitude of 2.7 has an average source duration of 0.16 and 0.14 seconds for station HSPB and HOPEN, respectively.

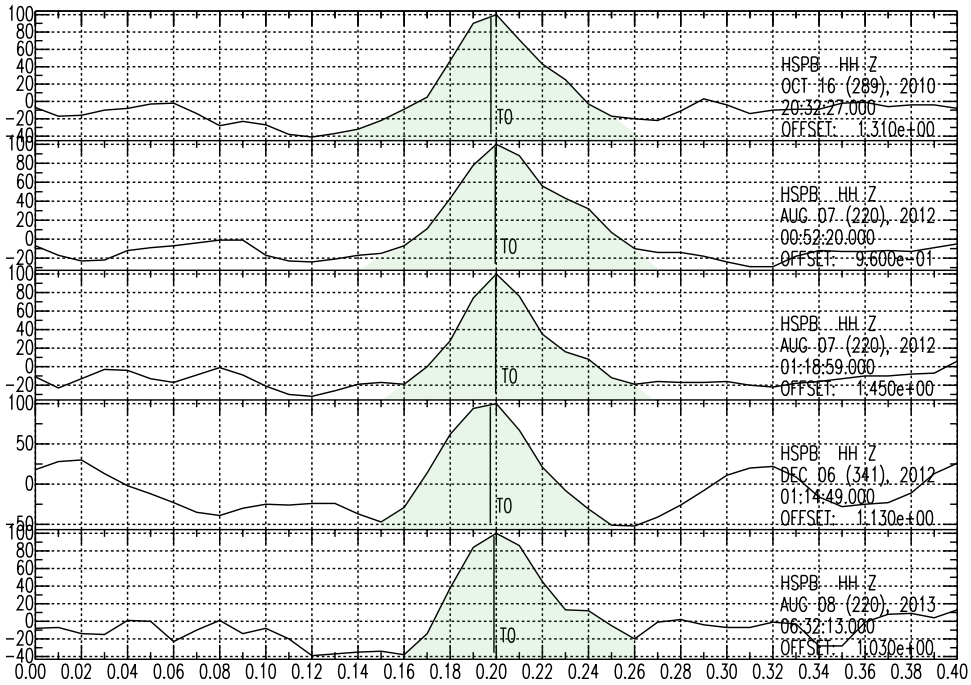

Figure 4.16: The source time function of the earthquake on 6 December 2012 at 21:11 with a magnitude of 2.3 has an average source duration of 0.12 seconds.

However, for those events in which a clear and consistent shape is obtained using several different EGFs, it is possible to measure more precise source durations and the subsequent calculations can be carried out more confidently. This is the case for ten master events with a M_L magnitude ranging from 2.3 to 3.3. The source time functions of these master events are isolated through deconvolution using smaller events with a M_L magnitude ranging from 0.9 to 2.0 as empirical Green's functions. The source parameters are only based on the source time functions obtained at HSPB station, as this is the only station in which seismic moment could be derived.

For comparison, the other parameters are also derived using spectral fitting. These values are displayed in the four last columns in Table 4. For earthquakes of the size of the events used in this study, it will often be difficult to get the correct corner frequency from the displacement spectra without correction for geometrical spreading and near surface attenuation. Visual inspection is also important to confirm the noise level and then to set the proper frequency range (Havskov and Ottemöller, 2010). The corner frequencies (f_{c-spec}) and stress drop (σ_{spec}) values derived from displacement spectra are fairly low, but correspond to those resulting from the EGF method, that should also give the most reliable results. The stress drop values fall within a range of 0.1-1.5 bar, where the highest

stress drop values are caused by the largest earthquakes.

Seeing that no events with a magnitude above 3.3 could be correlated with the other events, the outcome from the EGF analysis is limited to only a small range of magnitudes. For that reason, it might be worth to evaluate these results in the context of results from previous studies. Ottemöller et al. (2014) derived source parameters for larger earthquakes in Storfjorden (M_w 3.2 to 6.2) using the grid search technique of Ottemöller and Havskov (2003). An average stress drop value, seismic moment and corner frequency was obtained for 30 earthquakes and the result is given in Figure 4.17 and in Figure 4.18. The stress drop values range from 194-5 bar, with an average of 46 bar. Hence, most of them are considerably higher than the estimates from this work, which has been added to the same figures, indicated by the red circles. Additionally, six more events from 2015-2016 are added, ranging in size from M_w 3.3 to 3.8 and with stress drop values between 13.5 to 75.7 bar, giving a total of 46 events. From this it might be suggested that stress drop decrease with decreasing seismic moment and that earthquake self-similarity breaks down for smaller magnitude events. It may also be that the apparent decrease of stress drop is due to errors in the stress drop estimates, and that over this range of magnitudes there is a constant stress drop, in favour of the theory of earthquake self-similarity. Further discussion will be made in the next chapter.

#	Cluster	Date	Time	Lat	Lon	Depth	M_L	T	f_c	a	σ	M_0	f_{c-spec}	a_{spec}	σ_{spec}	M_w
		(ddmmyyyy)	(hhmm)	(°N)	(°E)	(km)		(s)	(Hz)	(km)	(bars)	(Nm)	(Hz)	(km)	(bar)	
1	3	29022012	1555	76.9461	18.6597	19.444	3.2	0.18	1.8	0.74	1.1	1.0E14	2.1	0.6	1.3	3.3
2	3	08042012	0135	76.9563	18.8454	9.945	2.7	0.15	2.1	0.63	0.2	1.0E13	3.1	0.4	0.5	2.7
3	3	06122012	2111	76.9513	18.7460	21.568	2.3	0.12	2.7	0.50	0.3	1.0E13	3.4	0.4	0.5	2.4
4	4	28062016	0531	76.8802	18.3681	13.321	3.0	0.17	1.9	0.70	1.3	1.0E14	2.0	0.6	0.6	3.0
5	4	22022012	1641	76.9102	18.2705	11.246	2.7	0.14	2.3	0.57	0.2	1.0E13	3.1	0.4	1.0	2.8
6	7	07082013	1515	76.9496	18.8666	11.453	2.5	0.14	2.3	0.57	0.2	1.0E13	3.9	0.4	0.9	2.6
7	10	12012016	0048	76.8839	18.3838	13.841	3.3	0.18	1.8	0.74	1.1	1.0E14	3.0	0.4	2.3	3.1
8	17	23062011	0828	77.1190	18.6918	15.331	3.0	0.16	2.0	0.67	1.5	1.0E14	2.6	0.9	0.6	3.2
9	17	24062012	1827	77.1587	18.7854	10.034	2.9	0.14	2.3	0.57	0.2	1.0E13	3.7	0.4	2.3	2.8
10	17	10072011	0014	77.1286	18.6379	21.510	2.6	0.13	2.5	0.53	0.3	1.0E13	3.4	0.4	0.9	2.7

Table 4: Estimated source parameters for a total of ten earthquakes that occur in five separate clusters of correlated events and recorded at the HSPB station. The five last columns represent values derived from the displacement spectra.

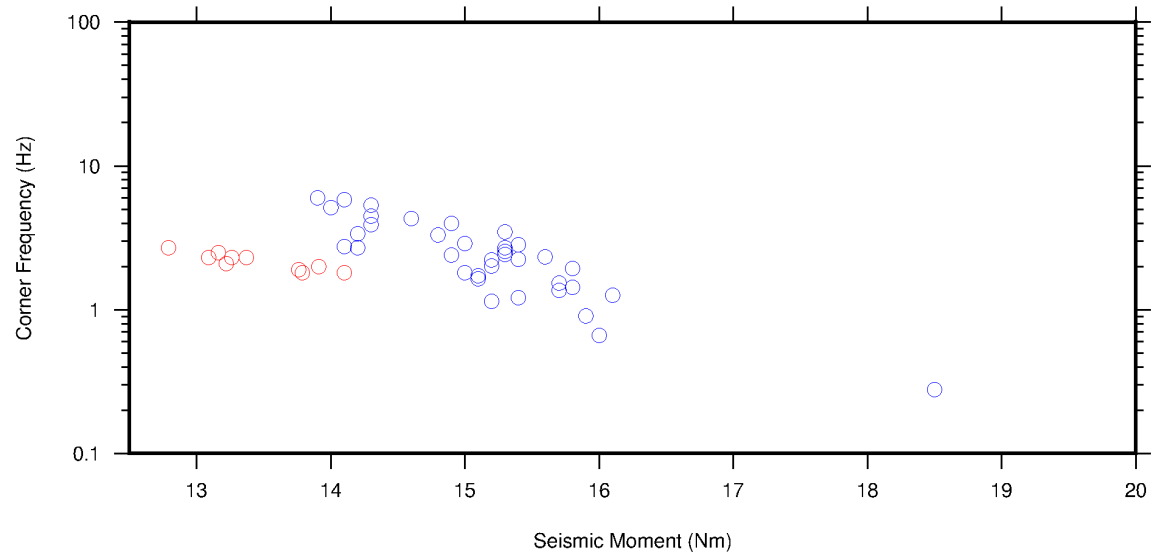

Figure 4.17: Scaling of corner frequency (f_c) with seismic moment (M_0) for the small earthquakes in this study (red circles) and for the larger earthquakes (blue circles) obtained in the study by Ottemöller et al. (2014), that nearly follows $M_0 \propto f_c^{-3}$ scaling in accordance with self-similar earthquakes (Kanamori and Rivera, 2004).

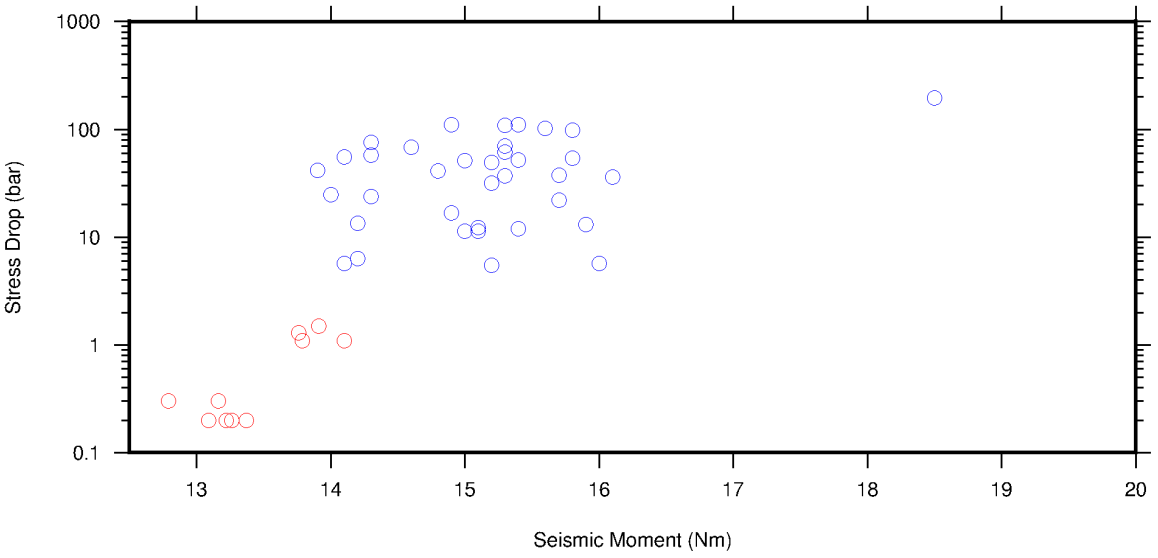

Figure 4.18: Stress drop (σ) versus seismic moment (M_0). Comparison of stress drop values obtained in the EGF analysis (red circles) with the ones obtained by the grid search method (blue circles).

5 Discussion and Interpretation

This chapter discuss the results and implications of the double-difference relocation and the empirical Green's function analysis for the earthquakes occurring in Storfjorden. The results will be compared to previous studies and reviewed within the geotectonic context.

5.1 Evaluation and implications of HypoDD results

Improved earthquake locations were obtained for the Storfjorden sequence using a double-difference relocation and waveform cross-correlation technique. These methods minimized the location uncertainty caused by errors in arrival times and in the velocity model. The double-difference location program computes formal errors for each hypocenter assuming an arrival time error of 0.1 seconds. However, relative errors were also estimated by adding random noise to the P and S-arrival times, which resulted in an average error in relative hypocenter location of $\sim$ 1141 m in the east-west direction, $\sim$ 1644 m in the north-south direction, and $\sim$ 2165 m in the vertical direction (see Table 5). These errors are slightly larger than the individual formal errors, which are smaller and possibly underestimated (Paige and Saunders, 1982). Though, both indicate that the relative location error is of the order of 1-2 km. A limiting factor is the number and geometry of the seismic stations, which is considered sparse and unfavourable for this region. However, it is clear that the relocation results in an improved image of seismicity as we start to see clear features and find an improvement in the relocation of clusters with events that have highly correlated waveforms.

P and S arrival times (s)	Standard deviation (x, y, z) in m		
P(0.1) S(0.2)	692.48	1011.43	1291.73
P(0.2) S(0.4)	1141.09	1644.31	2164.71
P(0.4) S(0.8)	1886.02	2723.56	3406.48

Table 5: The result of adding random noise to P and S-arrival times using 100 repetitions.

About one quarter of the relocated events are cross-correlated events, but the use of relative arrival time picks based on cross correlation does not have a large impact on the final relocations. From the results of the relocation process, by allowing different

maximum hypocentral distances between earthquakes, a maximum separation of 10 km between events was favoured. This value was believed to give the overall best balance between number of events and stability, as well as the most useful improvement of the initial locations.

The relocated events are mainly located within two clusters. The first cluster contains the majority of the events and therefore is referred to as the main cluster. The second cluster, that became active only in 2016, is located approximately 100 km north-east of the main cluster centroid. The initial locations were refined and it was possible to identify at least four linear features, interpreted as faults, within the main cluster that indicate a NE-SW trend of seismicity. The same trend is observed for a linear feature within the second cluster, possibly being the north-easterly extension of the fault zone. Cross-sections were made across and along the apparent fault plane and here show indications of steeply dipping structures to the south-east and that the activity in general does not occur at a depth larger than 30 km. This trend matches one of the nodal planes from the moment tensor inversion and likely is the dominant strike direction of the faults. However, the obtained fault plane solutions also suggests other fault directions. Therefore, I considered NW-SE striking faults, that revealed an apparent dip to the south-west. This can be associated with the normal faulting that appear to occur in this part of the fault zone.

The temporal and spatial evolution of the sequence from 2008 until 2016 has been presented and reveals clear migration patterns. A significant part of the seismicity is centred around the hypocenter of the M_w 6.1 magnitude event located within the main cluster. Two years after the mainshock, the activity migrates to the south-west, a part of the sequence that remains active also in the following year. From year 2012 until 2015, the seismicity occur mainly in the area of the mainshock, but with some scattered activity towards north and west. In 2016, a significant change in the number of earthquakes and location follows the M_w 5.2 event. This marks the onset of the increased seismicity in the north-east, as well as an indication of the existence of a larger fault zone that extends to the north-east.

5.2 Stress drop for Storfjorden events

Ottemöller et al. (2014) determined source parameters for M_w 3.2 to 6.2 events in Storfjorden using an automatic grid search technique. The stress drops ranged from 5 to 194

bar, for seismic moments of 7.9×10^{13} to 3.2×10^{18} Nm. The uncertainties in the spectral fitting approach increase for smaller events due to, possibly, insufficient correction for attenuation towards higher frequency. In this study it was extended to smaller events (M_L 2.5 to 3.3) using the empirical Green's function technique. For a collection of ten earthquakes, the effects from path, site and instrument was successfully removed by spectral division in the frequency domain. This was feasible as the events in the sequence are correlated and recorded at a common station. The source pulse duration was measured and used in the calculation of source parameters. All the earthquakes are associated with low stress drop, ranging from 0.2 to 1.5 bar. For comparison, source parameters were derived from displacement spectra for the same events and gave corresponding stress drop values ranging from 0.5 to 2.3 bar. This was considered as a confirmation that the EGF method works and also that the results obtained for the larger events based on spectral fitting are reliable. The stress drops from both methods are plotted against seismic moment, as displayed in Figure 4.18. With an average of 48 bar, it is evident that the larger earthquakes have significantly higher stress drop values compared to the smaller events analysed in this study. It should also be noted that the M_w 6.2 main event is distinguished by having the largest stress drop in the sequence, that corresponds well with the generally high stress drop values ($\sim$ 100 bar) observed for intraplate earthquakes (Kanamori and Anderson, 1975). Even considering the fairly large uncertainties in stress drop estimates, these differences are quite significant.

A subject of major controversy in seismology is that of earthquake scaling, which is important for the understanding of earthquake physics and in estimating seismic hazard (Stirling et al., 2013). Constant stress drop scaling or earthquake self-similarity for all magnitudes has been proposed in a number of studies (Aki, 1967; Ide and Beroza, 2001; Ide et al., 2003), and implies that all earthquakes are similar in their ratio of slip to fault size. Observations of stress drop often vary between 10 and 100 bar within the same tectonic environment (Stein and Wysession, 2003). In this work, however, there appears to be a decrease in the stress drop with decreasing seismic moment, possibly reflecting varying fault properties for these earthquakes.

In a study by Archuleta et al. (1982) of earthquakes in the Mammoth Lakes area, California, an apparent breakdown of constant stress was seen for the smaller earthquakes in the sequence. The study was based on a selection of earthquakes that span six orders of

magnitude in seismic moment. It was revealed that for seismic moment above 10^{21} dyn-cm, stress drop was constant in the range between 10 and 100 bar, with an average value of about 50 bar. On the other hand, for smaller seismic moments, stress drop seemed to be decreasing with moment (Figure 5.1).

In another study, Abercrombie (1995) found constant stress drop over the whole range of magnitudes using earthquakes with magnitude -1 to 5 M_L recorded at 2.5 km depth in the Cajon Pass borehole in California. She argued that there is no breakdown of self-similarity for smaller magnitude events. However, in the same study it was also found that the apparent stress (rigidity times ratio of radiated seismic energy to seismic moment) was decreasing with decreasing seismic moment over the same range. Stress drop and apparent stress that varies differently with seismic moment was also discovered by Prejean and Ellsworth (2001) in a more recent study. Abercrombie (1995) and Ide and Beroza (2001), among others, have argued that this non-constant scaling relationship is due to limited bandwidth or strong near surface attenuation for small events, which will underestimate the corner frequency and stress drop.

In this case, the use of the EGF method remove the effect of near surface attenuation. Also, it does not suffer from limited bandwidth as the corner frequency of the smaller event is not seen in the deconvolution. However, one does not get beyond the fact that stress drop estimates are prone to a large uncertainty as it is inversely proportional to the cube of source radius according to the Brune (1970) model. Therefore a small error in the corner frequency can lead to large errors in stress drop (Stein and Wysession, 2003). There also is some uncertainty related to the seismic moment. However, this can usually be determined more accurately, and within a factor of two for larger events (Kanamori and Anderson, 1975).

Whether this wide range of stress drop values is related to the errors in the calculations or actually reflects true source differences within the earthquake zone has important implications. It seems that the largest event initiated the sequence by reactivating a fault system and that this event is associated with the highest stress drop. Once the area is activated due to the movement and associated stress changes of the larger events, the lower stress drop indicates that the smaller events occur more easily. The moderate size earthquakes are somewhere in between. Including more and larger correlated events in the EGF analysis would be useful in order to verify the quality of the results. However, it

appears that the moderate size earthquakes in the sequence are not well enough correlated with other events.

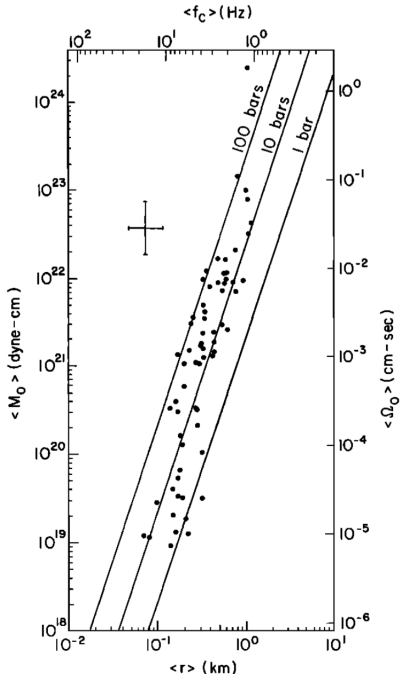

Figure 5.1: The study of 67 earthquakes in the Mammoth Lakes implies a breakdown in earthquake self-similarity for events with a seismic moment of less than about 10^{21} dyne-cm, while the larger events have a constant stress drop of about 50 bar over the range of magnitudes (Archuleta et al., 1982).

5.3 Geotectonic context

The seismic activity in Storfjorden indicates the presence of several tectonic structures, in which some have a clear NE-SW trend, while others occur as clusters with no obvious trend. The NE-SW trend deviates from the NNW-SSE trend of the major mapped faults dominating the area in the south and the NS structure to the north (Figure 2.2). Assuming that there are NE-SW striking faults, the profiles that were made across the probable fault plane suggests vertical faults and faults steeply dipping to the south-east. This is also in agreement with what Pirli et al. (2010) found in their preliminary analysis of the sequence, where a spatial distribution of the aftershocks is presented and which correlates with the teleseismic moment tensor solution of the mainshock (M_w 6.1). Further work on the sequence by Pirli et al. (2013) gave similar results. Based on fault plane solutions, NW-SE striking faults were also suggested and indicate a dip direction to the south-west.

In former studies the faulting mechanism for the larger earthquakes in the sequence was determined through moment tensor inversion using both regional and teleseismic data. A first attempt using both regional and teleseismic observations was made for the mainshock and indicated an oblique-normal fault trending NE-SW and dipping to the SSE (Pirli et al., 2010). Moment tensor solutions for nine larger aftershocks ($M > 4.0$) ranges from strike-slip to normal faults. There is a tendency of nearly east-west trending normal faults towards the western and southwestern part of the main cluster, while NE-SW trending strike-slip faults and oblique-normal faults are found for the earthquakes in the eastern and north-eastern part (Pirli et al., 2013). The same trend has been observed for moment tensor solutions derived by Junek et al. (2014) and Ottemöller et al. (2014). Thus, the moment tensor solutions indicate that rupture occurs along at least two different directions in Storfjorden where the normal faults accommodate slip required due to the movement along the oblique normal faults.

The underlying cause of seismicity in Storfjorden can be considered by addressing the sources of stress in the Svalbard region. As mentioned, it is likely that both regional and local factors affect the tectonic system. This is also indicated by the fault plane solutions that have been described. Ottemöller et al. (2014) used the fault plane solutions to invert for stress orientations. For 16 earthquakes a general E-W trending P-axis and NNW-SSE trending T-axis was found. A regional stress tensor also indicated a maximum principal stress axis (σ_1) following a general east-west trend with a plunge of 44°, in some cases almost vertical, and a minimum principal stress axis (σ_3) that has a north-south trend. This is consistent with the variety of fault plane solutions ranging from strike-slip to normal faulting and also in agreement with the results from other research (Junek et al., 2014; Pirli et al., 2013). The east-west stress orientation of (σ_1) deviates from the estimated regional stress originating from the plate boundaries, which might indicate that the regional stress pattern is more complicated. However, the influence of local stresses to explain the seismicity in this area should also be considered. One possible explanation for the observed extension is release of flexural stresses due to post-glacial isostatic uplift occurring on Svalbard, or sediment loading that can create stresses large enough to cause seismicity in case of rapid sedimentation where sediments are transported from Storfjorden to deeper ocean (Fejerskov and Lindholm, 2000). In combination with pre-existing zones of weakness it is possible that these vertical stresses can be the cause of normal faulting

earthquakes (Hicks et al., 2000). However, since the solutions also indicate strike-slip faults and oblique-normal faults, the impact from other factors needs to be considered as an alternative.

The Storfjorden earthquakes fall into an area of a complex tectonic structure and stress regime. The seismicity pattern indicates a fault system that is not related to any of the major mapped faults. However, the offshore extension of the faults into the Storfjorden area, that is, the Billefjorden Fault Zone (BFZ), the Lomfjorden Fault Zone (LFZ) and the Storfjorden Fault Zone (SFZ) is not known. Figure 5.2 gives an overview of mapped and inferred tectonic structures in the Storfjorden area, and indicates the location of the two seismic profiles: Horsted'05 (Czuba et al., 2008) and Profile 10 (Breivik et al., 2005). As noted in the figure, there are different interpretations of the offshore extension of the faults into Storfjorden. The inferred southern extension of BFZ (1 in Fig. 5.2) could not be observed on the Horsted'05 profile. The other interpretation (3 in Fig. 5.2) has been inferred by Breivik et al. (2005) based on seismic profiling. The Lomfjorden fault zone is a long-lived tectonic lineament. The last movement of which is thought to be in Late Paleogene. Strike-slip movement along a N-S trending fault have formed smaller intermediate structures with a different orientation which have had either reverse or normal movement throughout time (Dallmann, 2011). It is possible that the Storfjorden events can be related to this, or a similar structure, where there is strike-slip movement with normal-faulting blocks in between (Figure 5.4). Another observation by Edwards (1976) suggests the presence of growth faults in the nearly horizontal and undeformed Upper Triassic sedimentary rocks in the Mesozoic platform areas south on Edgeøya (13 in Fig. 5.2). Growth faults are extensional faults that can be caused by continuous deposition of sediments. They are observed in coastal cliffs at Kvalpynten and have an apparent dip to the south in most cases, but with an unknown strike. From geophysical data, the presence of a NE-SW trending structural high that is bounded by normal faults has been inferred (11 and 12 in Fig. 5.2) (Faleide et al., 1984). Also, a study by Bergh and Grogan (2003) suggests the existence of a Tertiary shear zone south of Spitsbergen with a NE-SW trend and possibly continuing into Storfjorden (10 in Fig. 5.2). This zone could be seen as a possible explanation for the observed migration of hypocenters to the south-west in Storfjorden. However, its existence has not been confirmed by mapping so the extent of this zone remains unknown. The prolongation of the Storfjorden Fault Zone

is believed to extend in a southern direction (Dallmann, 2015).

Savostin and Karasik (1981) suggested the existence of a Spitsbergen microplate between the Eurasian and North-American lithospheric plates in order to explain the seismicity in the Norwegian/Greenland Sea. Two different models were suggested: one that consists of a small lithospheric block with a western boundary at the Knipovich ridge, bounded in the south by the seismic belt in the Norwegian/Greenland Sea and an eastern boundary that follows the trend of Eurekan deformation and joins the Spitsbergen Fracture Zone (Figure 5.3a). Instead of a north-western extension, the second model suggests a plate boundary that extends from the ridge to the west and continuous towards the north-east through southern Spitsbergen and towards Franz Josef Land and terminates at the Gakkel ridge in the north (Figure 5.3b). The north-eastern extension of the boundary was based on a few events in Heer Land and in Franz Josef Land and is therefore considered rather speculative.

While the existence of a Spitsbergen microplate is rather uncertain, the increased activity in Storfjorden since 2008, and particularly the more recent activity in 2016 which marks the north-eastern extension of the sequence, suggests a rather large and complex fault zone in this area. The activity may be associated with pull-apart tectonics as would be expected during the early stages of rifting. In order to resolve these questions, acquisition and monitoring of new GPS data, as well as stress modelling is needed.

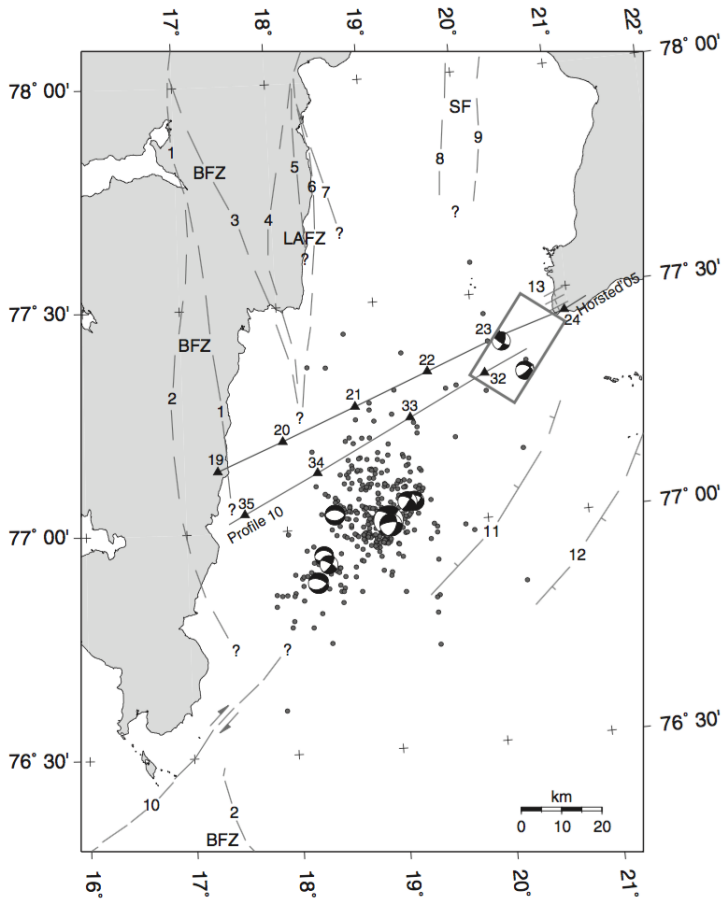

Figure 5.2: Inferred structures in Storfjorden and the two seismic profiles Horsted'05 and Profile 10. Number 1-9 are different interpretations of the offshore extension of Billefjorden, Lomfjorden and Storfjorden Fault Zones. The number 10 indicates the inferred Tertiary shear zone, 11-12 are the NE-SW trending ridge bounded by normal faults and 13 indicate Triassic growth faults (Pirli et al., 2013).

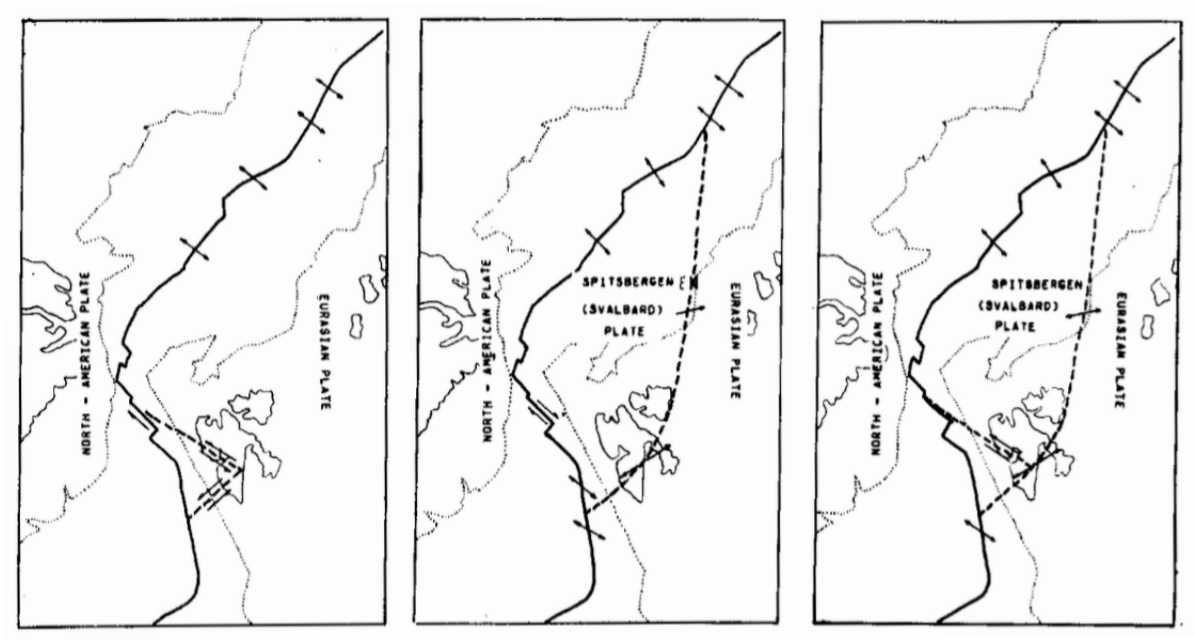

Figure 5.3: Different models of the Spitsbergen microplate. (a) smaller block bordered by the Knipovich Ridge, the seismic belt to the south and the Spitsbergen Fracture Zone. (b) a larger hypothetical plate boundary is bordered by the Knipovich and Gakkel ridge, as well as a seismic zone extending from south. (c) a combined version of the suggested boundaries (Savostin and Karasik, 1981).

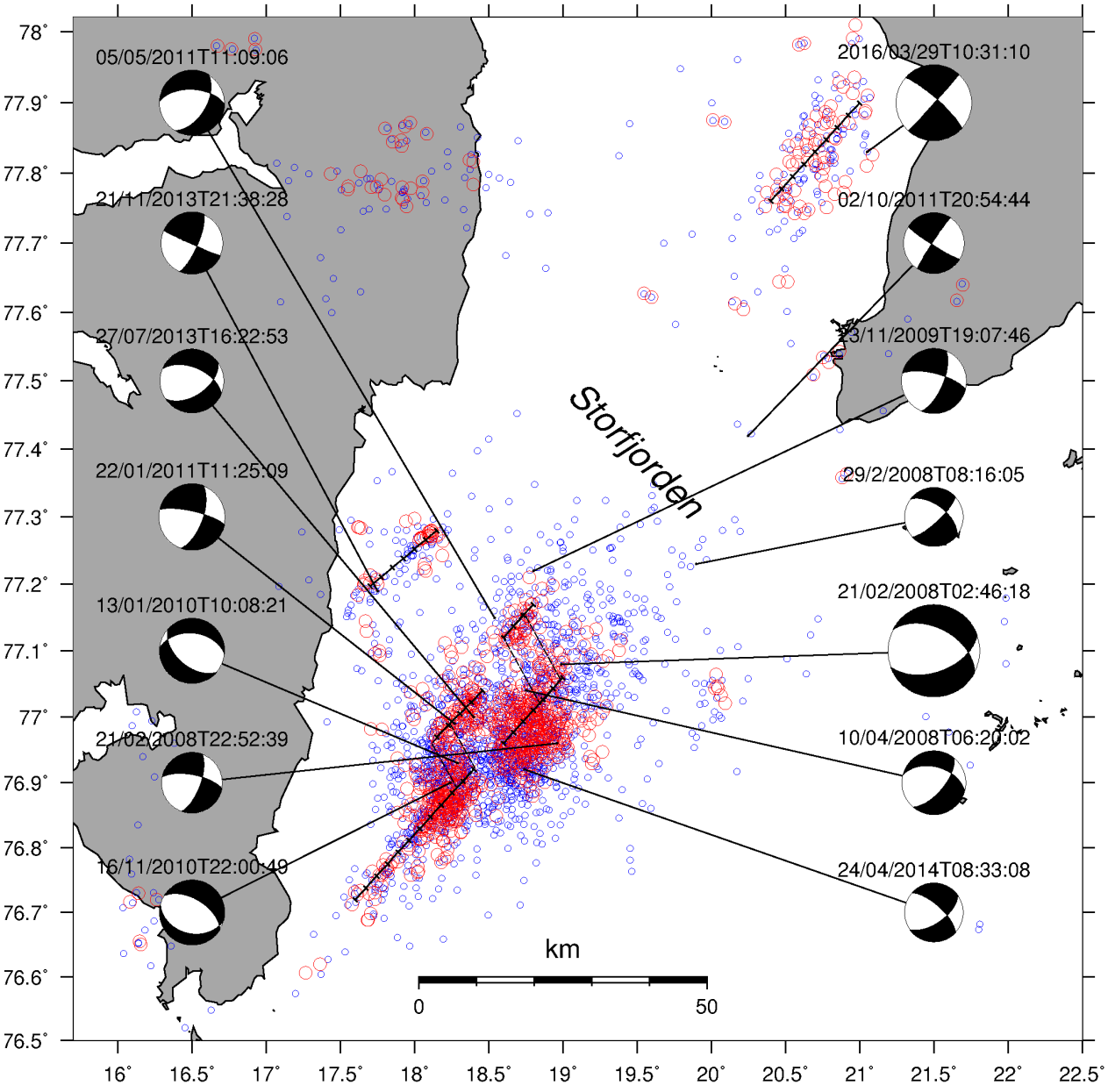

Figure 5.4: Interpretation of structures in Storfjorden with fault plane solutions from Ottemöller et al. (2014). SW-NE trending strike-slip faults accompanied by pull-apart structures (dashed lines) that explain the normal faulting.

6 Conclusions

The Storfjorden activity is a significant intraplate earthquake sequence that occurs in northern Europe. Using the seismic stations on the Svalbard archipelago, the activity is reasonably well monitored. I used these data to obtain an improved image of the earthquake distribution between 2008 and 2016, and to obtain a better understanding of their physical properties and causes. This resulted in the following main conclusions:

- The double-difference relocation algorithm applied to the earthquake sequence in Storfjorden clearly improves the initial hypocenter locations and reveals at least four NE-SW trending structures within the seismic zone. The quality of the relocations are verified by adding random noise to the arrival times to estimate the relative location error.

- Temporal distribution of the sequence reveals migration of hypocenters to the south-west and north-east, as well as more diffuse activity to the north and west of the largest cluster.

- Profiles across the NE-SW linear features indicate steeply dipping structures to the south-east that are constrained to the uppermost 10-25 km of the crust and possibly NW-SE oriented structures that show an apparent dip to the south-west. A possible explanation is a fault system of NE-SW strike-slip faults accompanied by intermediate oblique-normal faults.

- Path, site and instrument effects are removed from the seismogram of larger events by using smaller correlated events as empirical Green's functions. The deconvolved source pulse is used in estimating corner frequency, source radius and stress drop.

- Plots of seismic moment against stress drop reveals an apparent decrease of stress drop with decreasing seismic moment and implies a breakdown of earthquake self-similarity for smaller magnitude events in the Storfjorden earthquake sequence.

- The large difference in stress drop between larger and smaller earthquakes indicates differences in fault properties. The low stress drop for correlated events suggests the presence of secondary activations that are triggered more easily due to lower fault strength.

- The activity in Storfjorden can be linked to pre-existing zones of weakness in a structurally complex area which are being reactivated under the present state of stress. Both the influence of local and regional stresses have to be considered, but so far the exact underlying causes are not understood.

- There is no conclusive evidence for the existence of a plate boundary. Although, the activity is possibly similar to what is expected during early rifting.

References

Abercrombie, R. E. (1995), 'Earthquake source scaling relationships from -1 to 5 ML using seismograms recorded at 2.5-km depth', *Journal of Geophysical Research* **100**(B12), 24,015–24,036.

Aki, K. (1967), 'Scaling Law of Seismic Spectrum', *Journal of Geophysical Research* .

Ammon, C. J. (1991), 'The Isolation of Receiver Effects from Teleseismic P Waveforms', *Bulletin of the Seismological Society of America* **81**(6), 2504–2510.

Archuleta, R. J., Cranswick, E., Mueller, C. and Spudich, P. (1982), 'Source Parameters of the 1980 Mammoth Lakes, California, Earthquake Sequence', *Journal of Geophysical Research* **87**(B6), 4595–4697.

Austegard, A. (1976), 'Earthquakes in the Svalbard area', *Norsk Polarinstitutt, Årbok 1974* pp. 83–99.

Benz, H. M. and Herrmann, R. B. (2014), 'Rapid Estimates of the Source Time Function and M_w using Empirical Green's Function Deconvolution', *Bulletin of the Seismological Society of America* **104**(4), 1812–1819.

Bergh, S. G. and Grogan, P. (2003), 'Tertiary structure of the Sørkapp-Hornsund Region, South Spitsbergen, and implications for the offshore southern extension of the fold-thrust Belt', *Norwegian Journal of Geology* **83**, 43–60.

Breivik, A. J., Mjelde, R., Grogan, P., Shimamura, H., Murai, Y. and Nishimura, Y. (2005), 'Caledonide development offshore–onshore Svalbard based on ocean bottom seismometer, conventional seismic, and potential field data', *Tectonophysics* **401**, 79–117.

Brune, J. N. (1970), 'Tectonic Stress and the Spectra of Seismic Shear Waves from Earthquakes', *Journal of Geophysical Research* **75**(26), 4997–5009.

Bryhni, I., Nøttvedt, A., Ramberg, I. B. and Rangnes, K. (2013), *Landet blir til: Norges geologi*, Norsk Geologisk Forening.

Bungum, H., Mitchell, B. and Kristoffersen, Y. (1982), 'Concentrated earthquake zones in Svalbard', *Tectonophysics* **82**, 175–188.

Bungum, H., Olesen, O., Pascal, C., Gibbons, S., Lindholm, C. and Vestøl, O. (2010), 'To what extent is the present seismicity of Norway driven by post-glacial rebound?', *Journal of Geological Society* **167**, 373–384.

Castellanos, F. and van der Baan, M. (2013), 'Microseismic Event Locations using the Double-Difference Algorithm', *Canadian Journal of Exploration Geophysics* **38**(3).

Chan, W. W. and Mitchell, B. (1985), 'Intraplate earthquakes in northern Svalbard', *Tectonophysics* **114**, 181–191.

Clayton, R. W. and Wiggins, R. A. (1976), 'Source shape estimation and deconvolution of teleseismic bodywaves', *Geophys. J. R. Astron Soc.* **47**, 151–177.

Czuba, W., Grad, M., Guterch, A., Majdanski, M., Malinowski, M., Mjelde, R., Moskalik, M., Sroda, P., Wilde-Piorko, M. and Nishimura, Y. (2008), 'Seismic crustal structure along the deep transect Horsted'05, Svalbard', *Polish Polar Research* **29**(3), 279–290.

Dallmann, W. K. (2011), 'Gamle forkastninger i Svalbards jordskorpe fortsatt aktive'. **URL:** *http://www.npolar.no/no/kronikker/2011/2011-01-11-gamle-forkastinger-fortsatt-aktive.html (last accesses 10.04.2017)*

Dallmann, W. K., ed. (2015), *Geoscience Atlas of Svalbard*, Rapportserie nr: 148, Norsk Polarinstitutt.

Douglas, A. (1967), 'Joint epicenter determination', *Nature* **215**, 47–48.

Edwards, M. B. (1976), 'Growth Faults in Upper Triassic Deltaic Sediments, Svalbard', *The American Association of Petroleum Geologists Bulletin* **60**(3), 341–355.

Faleide, J. I., Gudlaugsson, S. T. and Jacquart, G. (1984), 'Evolution of the western Barents Sea', *Marine and Petroleum Geology* **1**, 123–150.

Fejerskov, M. and Lindholm, C. D. (2000), Crustal stress in and around Norway: an evaluation of stress-generating mechanisms, *in* A. e. a. Nødttvedt, ed., 'Dynamics of the Norwegian Margin', Vol. Special Publications 167, Geological Society of London, pp. 451–467.

Forman, S. L., Lubinski, D. J., Ingólfsson, Ó., Zeeberg, J., Snyder, J., Siegert, M. and Matishov, G. (2004), 'A review of postglacial emergence on Svalbard, Franz Josef Land and Novaya Zemlya, northern Eurasia', *Quaternary Science Reviews* **23**, 1391–1434.

Hartzell, S. H. (1978), 'Earthquake Aftershocks as Green's Functions', *Geophysical Research Letters* **5**(1).

Havskov, J. and Bungum, H. (1987), 'Source parameters for earthquakes in the northern North Sea', *Norsk Geologisk Tidsskrift* **67**, 51–58.

Havskov, J. and Ottemöller, L. (2010), *Routine Data Processing in Earthquake Seismology*, Springer Netherlands.

Hicks, E. C., Bungum, H. and Lindholm, C. D. (2000), 'Seismic activity, inferred crustal stresses and seismotectonics in the Rana region, Northern Norway', *Quaternary Science Reviews* **19**, 1423–1436.

Husebye, E., Gjøystdal, H., Bungum, H. and Eldholm, O. (1975), 'The seismicity of the Norwegian and Greenland Seas and adjacent continental shelf areas', *Tectonophysics* **26**, 55–70.

Husen, S. and Hardebeck, J. (2010), 'Earthquake location accuracy, Community Online Resource for Statistical Seismicity Analysis, doi: 10.5078/corssa-55815573'.

Hutchings, L. and Viegas, G. (2012), Application of Empirical Green's Functions in Earthquake Source, Wave Propagation and Strong Ground Motion Studies, *in* S. D'Amico, ed., 'Earthquake Research and Analysis - New Frontiers in Seismology', InTech.

Ide, S. and Beroza, G. C. (2001), 'Does apparent stress vary with earthquake size?', *Geophysical Research Letters* **28**(17), 3349–3352.

Ide, S., Beroza, G. C., Prejean, S. G. and Ellsworth, W. L. (2003), 'Apparent break in earthquake scaling due to path and site effects on deep borehole recordings', *Journal of Geophysical Research* **108**(B5), 2271.

Jakobsson, M., Mayer, L., Coakley, B., Dowdeswell, J. A., Forbes, S., Fridman, B., Hodnesdal, H., Noormets, R., Pedersen, R., Rebesco, M., Schenke, H. W., Zarayskaya, Y., Accettella, D., Armstrong, A., Anderson, R. M., Bienhoff, P., Camerlenghi, A., Church,

I., Edwards, M., Gardner, J. V., Hall, J. K., Hell, B., Hestvik, O., Kristoffersen, Y., Marcussen, C., Mohammad, R., Mosher, D., Nghiem, S. V., Pedrosa, M. T., Travaglini, P. G. and Weatherall, P. (2012), 'The International Bathymetric Chart of the Arctic Ocean (IBCAO) Version 3.0', *Geophysical Research Letters* **39**(L12609).

Junek, W. N., Kværna, T., Pirli, M., Schweitzer, J., Harris, D. B., Dodge, D. A. and Woods, M. T. (2015), 'Inferring Aftershock Sequence Properties and Tectonic Structure Using Empirical Signal Detectors', *Pure and Applied Geophysics* **172**, 359–373.

Junek, W. N., Roman-Nieves, J. I. and Woods, M. T. (2014), 'Tectonic implications of earthquake mechanisms in Svalbard', *Geophysical Journal International* **196**, 1152–1161.

Kanamori, H. and Anderson, D. L. (1975), 'Theoretical basis of some empirical relations in seismology', *Bulletin of the Seismological Society of America* **65**(5), 1073–1095.

Kanamori, H. and Rivera, L. (2004), 'Static and dynamic scaling relations for earthquakes and their implications for rupture speed and stress drop', *Bulletin of the Seismological Society of America* **94**(1), 314–319.

Landvik, J. Y., Bondevik, S., Elverhøi, A., Fjeldskaar, W., Mangerud, J., Salvigsen, O., Siegert, M. J., Svendsen, J. I. and Vorren, T. O. (1998), 'The last glacial maximum of Svalbard and the Barents Sea area: ice sheet extent and configuration', *Quaternary Science Reviews* **17**, 43–75.

Langston, C. A. (1979), 'Structure Under Mount Rainier, Washington, Inferred From Teleseismic Body Waves', *Journal of Geophysical Research* **84**(B9), 4749–4762.

Mitchell, B. and Chan, W.-W. W. (1978), 'Characteristics of Earthquakes in the Heerland Seismic Zone of Eastern Spitsbergen', *Polarforschung* **48**, 31–40.

Mitchell, B. J., Bungum, H., Chan, W. W. and Mitchell, P. B. (1990), 'Seismicity and present-day tectonics of the Svalbard region', *Geophysical Journal International* **102**(1), 139–149.

Mitchell, B., Zollweg, J. E., Kohsmann, J. J., Cheng, C.-C. and Haug, E. J. (1979), 'Intraplate earthquakes in the Svalbard archipelago', *Journal of Geophysical Research* **84**(B10), 5620–5626.

Mori, J. and Frankel, A. (1990), 'Source parameters for small events associated with the 1986 North Palm Springs, California, earthquake determined using empirical green functions', *Bulletin of the Seismological Society of America* **80**(2), 278–295.

Mueller, C. S. (1985), 'Source pulse enhancement by deconvolution of an empirical Green's function', *Geophysical Research Letters* **12**(1), 33–36.

Myers, S. C., Johannesson, G. and Hanley, W. (2007), 'A Bayesian hierarchical method for multiple-event seismic location', *Geophysical Journal International* **171**, 1049–1063.

Okino, K., Curewitz, D., Asada, M., Tamaki, K., Vogt, P. and Crane, K. (2002), 'Preliminary analysis of the Knipovich Ridge segmentation: influence of focused magmatism and ridge obliquity on an ultraslow spreading system', *Earth and Planetary Science Letters* **202**, 275–288.

Ottemöller, L. and Havskov, J. (2003), 'Moment Magnitude Determination for Local and Regional Earthquakes Based on Source Spectra', *Bulletin of the Seismological Society of America* **93**(1), 203–214.

Ottemöller, L., Kim, W. Y., Dallmann, W. and Waldhauser, F. (2014), Storfjorden intraplate earthquake sequence, 2008-2014. (Unpublished).

Ottemöller, L., Voss, P. and Havskov, J. (2014), *Seisan earthquake analysis software for Windows, Solaris, Linux and macOSX*.

Paige, C. C. and Saunders, M. A. (1982), 'LSQR: An Algorithm for Sparse Linear Equations and Sparse Least Squares', *ACM Transactions on Mathematical Software* **8**(1), 43–71.

Piepjohn, K., von Gosen, W., Läufer, A., McClelland, W. C. and Estrada, S. (2013), 'Ellesmerian and Eurekan fault tectonics at the northern margin of Ellesmere Island (Canadian High Arctic)', *Z. Dt. Ges. Geowiss* **164**(1), 81–105.

Piepjohn, K., von Gosen, W., Tessenohn, F., Reinhardt, L., McClelland, W. C., Dallmann, W., Gaedicke, C. and Harrison, J. C. (2015), 'Tectonic map of the Ellesmerian and Eurekan deformation belts on Svalbard, North Greenland, and the Queen Elisabeth Islands (Canadian Arctic)', *Arktos* **1**(1), 12.

Pirli, M., Schweitzer, J., Ottemöller, L., Raeesi, M., Mjelde, R., Atakan, K., Guterch, A., Gibbons, S. J., Paulsen, B., Debski, W., Wiejacz, P. and Kværna, T. (2010), 'Preliminary Analysis of the 21 February 2008 Svalbard (Norway) Seismic Sequence', *Seismological Research Letters* **81**(1), 63–75.

Pirli, M., Schweitzer, J. and Paulsen, B. (2013), 'The Storfjorden, Svalbard, 2008-2012 aftershock sequence: Seismotectonics in a polar environment', *Tectonophysics* **601**, 192–205.

Prejean, S. G. and Ellsworth, W. L. (2001), 'Observations of Earthquake Source Parameters at 2 km Depth in the Long Valley Caldera, Eastern California', *Bulletin of the Seismological Society of America* **91**(2), 165–177.

Savostin, L. and Karasik, A. (1981), 'Recent Plate Tectonics of The Arctic Basin and of Northeastern Asia', *Tectonophysics* **74**, 111–145.

Schaff, D. P., Bokelmann, G. H. R., Ellsworth, W. L., Zanzerkia, E., Waldhauser, F. and Beroza, G. C. (2004), 'Optimizing Correlation Techniques for Improved Earthquake Location', *Bulletin of the Seismological Society of America* **94**(2), 705–721.

Stange, S. and Schweitzer, J. (2004), 'Source depths at regional distances: an example from the western Barents Sea/Svalbard region', *NORSAR Scientific Report* **1**, 45–50.

Stein, S., Cloettngh, S., Sleep, N. H. and Wortel, R. (1989), Passive Margin Earthquakes, Stresses and Rheology, *in* S. Gregersen and P. W. Basham, eds, 'Earthquakes at North-Atlantic Passive Margins: Neotectonics and Postglacial Rebound', Kluwer Academic Publishers, pp. 231–259.

Stein, S. and Wysession, M. (2003), *An Introduction to Seismology, Earthquakes, and Earth Structure*, Blackwell Publishing.

Stirling, M., Goded, T., Berryman, K. and Litchfield, N. (2013), 'Selection of earthquake scaling relationships for seismic-hazard analysis', *Bulletin of the Seismological Society of America* .

Vallée, M. (2004), 'Stabilizing the Empirical green Function Analysis: Development of the Projected Landweber Method', *Bulletin of the Seismological Society of America* **94**(2), 394–409.

Velasco, A. A., Ammon, C. J. and Beck, S. L. (2000), 'Broadband source modeling of the November 8, 1997, Tibet (mw - 7.5) earthquake and its tectonic implications', *Journal of Geophysical Research* **105**(B12), 28,065–28,080.

Waldhauser, F. (2001), 'hypoDD - A Program to Compute Double-Differences Hypocenter Locations', *U.S Geol. Survey, Menlo Park, CA* .

Waldhauser, F. and Ellsworth, W. L. (2000), 'A double-difference earthquake location algorithm: Method and application to the northern hayward fault, California', *Bulletin of the Seismological Society of America* **90**(6), 1353–1368.

A Appendix

ph2dt input file (ph2dt.inp)

```
* ph2dt.inp - input control file for program ph2dt
* Input station file:
station.dat
* Input phase file:
phase.dat
*MINWGHT: min. pick weight allowed [0]
*MAXDIST: max. distance in km between event pair and stations [200]
*MAXSEP: max. hypocentral separation in km [10]
*MAXNGH: max. number of neighbors per event [10]
*MINLNK: min. number of links required to define a neighbor [8]
*MINOBS: min. number of links per pair saved [8]
*MAXOBS: max. number of links per pair saved [20] = nsta
*MINWGHT MAXDIST MAXSEP MAXNGH MINLNK MINOBS MAXOBS
    0     900     10      30     8      4     200
```

hypoDD input file (hypoDD.inp)

```
hypoDD_2
* RELOC.INP: <hypoDD2.inp>
*--- input file selection
* cross correlation diff times:
dt.cc
*
*catalog P diff times:
dt.ct
*
* event file:
event.dat
*
* station file:
station.dat
*
*--- output file selection
* original locations:
hypoDD.loc
* relocations:
hypoDD.reloc
* station information:
hypoDD.sta
* residual information:
hypoDD.res
* source paramater information:
hypoDD.src
*
*--- data type selection:
* IDAT:  0 = synthetics; 1= cross corr; 2= catalog; 3= cross & cat
* IPHA: 1= P; 2= S; 3= P&S
* MAXDIST: max dist [km] between cluster centroid and station
* IDAT   IPHA   MAXDIST
   3       3      900
*
*--- event clustering:
* OBSCC:    min # of obs/pair for crosstime data (0= no clustering)
* OBSCT:    min # of obs/pair for network data (0= no clustering; use 4 as default)
* MINDIST:  min pair-station distance (-9= not active)
* MAXDIST:  max pair-station distance (-9= not active)
* MAXGAP:   max azimuthal gap (-9= not active)
* OBSCC  OBSCT    MINDIST  MAXDIST  MAXGAP
    1      4       -999     -999    -999
*
*--- solution control:
* ISTART:       1 = from single source; 2 = from network sources
* ISOLV:        1 = SVD, 2=lsqr
* IAQ:          remove airquakes: 0=NO, 1=YES
* NSET:         number of sets of iteration with specifications following
```

```
*  ISTART  ISOLV  IAQ  NSET
    2       2     1    5
*
*--- data weighting and re-weighting:
* NITER:                last iteration to used the following weights
* WTCCP, WTCCS:         weight cross P, S
* WTCTP, WTCTS:         weight catalog P, S
* WRCC, WRCT:           residual threshold in sec for cross, catalog data
* WDCC, WDCT:           max dist [km] between cross, catalog linked pairs
* DAMP:                 damping (for lsqr only)
*       ---  CROSS DATA -----  ----CATALOG DATA ----
* NITER WTCCP WTCCS WRCC WDCC WTCTP WTCTS WRCT WDCT DAMP
  5     0.01 0.01  -999 -999  1.00  0.5    10 -999  100
  5     0.01 0.01  -999 -999  1.00  0.5     8    5   90
  5     1.0  0.5   -999 -999  1.00  0.5     8    5   70
  5     1.0  0.5      6    4  0.10  0.05    6    4   60
  5     1.0  0.5      6    4  0.01  0.005   6    4   50

*--- FORWARD MODEL:
* IMOD  0= 1D local, layered, P velocity w/ fixed vp/vs ratio (hypoDD1.0);
*       1= 1D local, layered, P velocity w/ variable vp/vs ratio
*       9= 3D local model (simulps raytracer)
0
*
*--- 1D model:
* NLAY:         number of model layers
* RATIO:        vp/vs ratio
* TOP:          depths of top of layer (km)
* VEL:          layer velocities (km/s)
* NLAY  RATIO
12     1.73
* TOP  VEL
0.00  2.00 4.00 8.00 12.0 16.0 20.0 23.0 27.0 31.0 40.0 50.0
* VEL
6.20  6.27 6.33 6.47 6.60 6.78 6.96 7.10 7.58 8.05 8.15 8.25
*
*--- event selection:
* CID:  cluste 0r to be relocated (0 = all)
* ID:   cuspids of event to be relocated (8 per line)
* CID
0
* ID
```

Outlier data from ph2dt.log

```
Outliers (STA,ID1,ID2,OFFSET (km),T1,T2,T1-T2)

Outlier: BJO1           3     2007    9.365   52.360   87.410  -35.050
Outlier: SPA0           6     1212    5.555    9.350   11.440   -2.090
Outlier: ARA0           7      218    4.669  111.850  109.650    2.200
Outlier: ARA0           7      218    4.669  192.970  188.750    4.220
Outlier: ARA0           7      244    4.871  192.970  188.970    4.000
Outlier: ARA0           7      852    5.269  111.850  109.920    1.930
Outlier: ARA0           7      852    5.269  192.970  188.450    4.520
Outlier: SPA0           7     1583    5.277   22.460   24.330   -1.870
Outlier: ARA0           7      173    5.587  192.970  189.720    3.250
Outlier: ARA0           7      303    7.033  111.850  108.820    3.030
Outlier: ARA0           7     1553    7.230  111.850  108.770    3.080
Outlier: ARA0           7      172    7.577  111.850  109.150    2.700
Outlier: ARA0           7      277    7.839  192.970  188.020    4.950
Outlier: ARA0           7     1531    9.455  111.850  108.260    3.590
Outlier: SPA0           8       45    0.873   19.320   21.450   -2.130
Outlier: HOPE           8       45    0.873   21.670   23.610   -1.940
Outlier: HOPE           8       45    0.873   41.650   42.690   -1.040
Outlier: ARA0           8       45    0.873  106.450  107.470   -1.020
Outlier: SPA0           8      272    0.981   19.320   21.280   -1.960
Outlier: HOPE           8      272    0.981   21.670   23.710   -2.040
Outlier: HOPE           8      272    0.981   41.650   43.050   -1.400
Outlier: KBS            8      272    0.981   34.360   35.910   -1.550
Outlier: ARA0           8      272    0.981  106.450  108.520   -2.070
Outlier: SPA0           8       29    1.171   19.320   21.510   -2.190
Outlier: HOPE           8       29    1.171   21.670   23.270   -1.600
Outlier: KBS            8       29    1.171   34.360   35.910   -1.550
Outlier: TRO            8       29    1.171  102.650  104.480   -1.830
Outlier: ARA0           8       29    1.171  106.450  107.550   -1.100
Outlier: HSPB           8     1954    1.489   10.710   12.980   -2.270
Outlier: HSPB           8     1954    1.489   20.050   24.350   -4.300
Outlier: SPA0           8     1954    1.489   19.320   21.410   -2.090
Outlier: HOPE           8     1954    1.489   41.650   44.490   -2.840
Outlier: KBS            8     1954    1.489   34.360   36.420   -2.060
Outlier: HSPB           8     1129    1.644   10.710   12.950   -2.240
Outlier: HSPB           8     1129    1.644   20.050   22.760   -2.710
Outlier: SPA0           8     1129    1.644   19.320   21.270   -1.950
Outlier: HOPE           8     1129    1.644   21.670   24.120   -2.450
Outlier: KBS            8     1129    1.644   34.360   36.090   -1.730
Outlier: ARA0           8     1129    1.644  106.450  108.620   -2.170
Outlier: SPA0           8      334    2.051   19.320   21.480   -2.160
Outlier: HOPE           8      334    2.051   41.650   45.330   -3.680
Outlier: KBS            8      334    2.051   34.360   36.260   -1.900
Outlier: ARA0           8      334    2.051  106.450  108.400   -1.950
Outlier: SPA0           8       84    2.253   19.320   21.000   -1.680
Outlier: HOPE           8       84    2.253   21.670   23.490   -1.820
Outlier: HOPE           8       84    2.253   41.650   45.170   -3.520
Outlier: HSPB           8     1156    2.267   10.710   12.470   -1.760
Outlier: HSPB           8     1156    2.267   20.050   25.260   -5.210
Outlier: SPA0           8     1156    2.267   19.320   21.740   -2.420
Outlier: HOPE           8     1156    2.267   21.670   25.390   -3.720
Outlier: HOPE           8     1156    2.267   41.650   44.570   -2.920
Outlier: HSPB           8     1955    2.368   10.710   12.860   -2.150
Outlier: HSPB           8     1955    2.368   20.050   24.250   -4.200
Outlier: SPA0           8     1955    2.368   19.320   21.310   -1.990
Outlier: HOPE           8     1955    2.368   41.650   44.580   -2.930
Outlier: KBS            8     1955    2.368   34.360   36.310   -1.950
Outlier: HSPB           8     1149    2.593   10.710   15.340   -4.630
Outlier: HSPB           8     1149    2.593   20.050   25.330   -5.280
Outlier: SPA0           8     1149    2.593   19.320   21.300   -1.980
Outlier: HOPE           8     1149    2.593   21.670   25.000   -3.330
Outlier: KBS            8     1149    2.593   34.360   36.400   -2.040
Outlier: ARA0           8     1149    2.593  106.450  110.150   -3.700
Outlier: SPA0           8      300    2.765   19.320   21.300   -1.980
Outlier: HOPE           8      300    2.765   41.650   44.800   -3.150
Outlier: KBS            8      300    2.765   34.360   36.230   -1.870
Outlier: ARA0           8      300    2.765  106.450  107.820   -1.370
Outlier: HSPB           8      377    2.821   20.050   21.920   -1.870
Outlier: SPA0           8      377    2.821   19.320   21.200   -1.880
Outlier: HOPE           8      377    2.821   21.670   23.470   -1.800
Outlier: HOPE           8      377    2.821   41.650   44.580   -2.930
Outlier: SPA0           8      870    2.827   19.320   21.360   -2.040
Outlier: HOPE           8      870    2.827   21.670   25.070   -3.400
Outlier: HOPE           8      870    2.827   41.650   43.600   -1.950
```

CORR input file (corr.inp)

```
# the program can do 2 things:
#
#    1) find correlated events, in this case comment out
#       parameter SFILE MASTER; program then correlates
#       all events and finds groups, output in file corr.out;
#       this should be done before 2 is attempted in
#       addition to visual inspection
#
#    2) pick phases in events by correlating with master event,
#       in this case define SFILE MASTER; program uses
#       parts of master event signals and computes correlation
#       for the remaining events; phase output is written to corr.out
#
#  trace file corr.trace gives additional info on the program run
#


KEYWORD.....Comments.....Par 1.....Par 2.....

SFILE INDEXFILE                         corr.lis

# minimum correlation value
MIN CORR                                0.8

# number of stations required for event pair to be correlated
MIN CORR CHAN                           2.

# either 0. or 1.
INTERACTIVE                             0.

# activate (1.) or deactivate (0.) filters set below
FILTER                                  1.

# time of window before phase as ratio of selected duration
PRE SIGNAL                              0.1

# use either full trace (0.) or same criteria as for master event (1.)
EVENT SELCRIT                           1.

# double sample rate n times
N DOUBLE SRATE                          0.

# time window for cross-correlation matrix, 999. for max
CC MATRIX WINDOW                        0.

# set hypocenter start latitude and longitude, 999. to not use
# (only affects output file, and use of location program afterwards)
START LATITUDE                          56.6
START LONGITUDE                         13.2

# set hypocenter fixed depth, 999. to not use
# (only affects output file, and use of location program afterwards)
FIX DEPTH                               5.

# keep original waveform names (0.) or put corr output file names (1.)
WAVENAME OUT                            0.

# output of correlation function, 0 for none,
# 1. for full data, 2 for reduced
# data 1 for data > MIN CORRELATION, otherwise 0
WAVE CORR OUT                           0.

# reduce to 0 (-) and 1 (+) if set to 1, full data if set to 1.
SINGLE BIT                              0.

# write out phases for correlation above threshold if set to 1.
CONTINUOUS MODE                         0.

# extract event files for correlation above threshold, 0. for no extract,
# 1. to extract single channel used, 2. extract all channels
CONTINUOUS EXTRACT                      0.

# flag to write corr.trace output file
TRACE OUTPUT                            0.
```

```
# maximum distance between event pair to compute correlation
MAX EVENT DISTANCE                      20.

# maximum distance between event and station
MAX STAT DISTANCE                       500.

# setup of stations
#   STAT, COMP    - station and component codes
#   SELCRIT       - 1=P, 2=S, 3=calc P, 4=calc S
#   DURATION      - signal duration in seconds if selcrit<4
#   FLOW, FHIGH   - filter limits for bandpass filter, can be
#                   disabled by FILTER (see above)
--------------------------------------------------------------------------
KEYWORD...STAT......COMP......SELCRIT...DURATION..FLOW......FHIGH.....

--- p ---
STATION   KBS       BH Z      1.        10.       2.        5.
STATION   KBS       BH N      4.        20.       2.        5.
STATION   KBS       BH E      4.        20.       2.        5.
STATION   KBS       BH 1      4.        20.       2.        5.
STATION   KBS       BH 2      4.        20.       2.        5.
STATION   HSPB      HH Z      1.        5.        2.        5.
STATION   HSPB      BH Z      1.        5.        2.        5.
STATION   HSP       BH Z      1.        5.        2.        5.
STATION   HSPB      HH N      4.        10.       2.        5.
STATION   HSPB      HH E      4.        10.       2.        5.
STATION   SPA0      BH Z      1.        8.        2.        5.
STATION   SPA0      BH Z      4.        20.       2.        5.

#STATION   BJ01      HH Z      1.        5.        2.        5.
#STATION   BJ01      BH Z      1.        5.        2.        5.
#STATION   BJ01      BHZ       1.        5.        2.        5.
```